Akkermansia muciniphila promotes type H vessels formation and bone fracture healing by reducing gut permeability and inflammation

Jiang-Hua Liu,[1,2] Tao Yue,[1,2] Zhong-Wei Luo,[1,2] Jia Cao,[2] Zi-Qi Yan,[2,7] Ling Jin,[1,2] Teng-Fei Wan,[1,2] Ci-Jun Shuai,[10] Zheng-Guang Wang,[8] Yong Zhou,[8]* Ran Xu,[9]* Hui Xie,[1,2,3,4,5,6]*

[1] Department of Orthopedics, Xiangya Hospital, Central South University, Changsha, Hunan, 410008, China.

[2] Movement System Injury and Repair Research Center, Xiangya Hospital, Central South University, Changsha, Hunan 410008, China.

[3] Department of Sports Medicine, Xiangya Hospital, Central South University, Changsha, Hunan 410008, China.

[4] Hunan Key Laboratory of Organ Injury, Aging and Regenerative Medicine, Changsha, Hunan 410008 China.

[5] Hunan Key Laboratory of Bone Joint Degeneration and Injury, Changsha, Hunan 410008, China.

[6] National Clinical Research Center for Geriatric Disorders, Xiangya Hospital, Central South University, Changsha, Hunan 410008, China.

[7] Department of Stomatology, Xiangya Hospital, Central South University, Changsha, Hunan 410008, China.

[8] Department of Orthopedics, the Third Xiangya Hospital, Central South University, Changsha, Hunan 410013, China.

[9] Department of Urology, the Second Xiangya Hospital, Central South University, Changsha, Hunan 410008, China.

[10] State Key Laboratory of High Performance Complex Manufacturing, College of Mechanical and Electrical Engineering, Central South University, Changsha, Hunan 410008, China.

*Corresponding author: Hui Xie (huixie@csu.edu.cn), Ran Xu (xuran@csu.edu.cn) and Yong Zhou (zhouyong1028@sina.com)

Key words: *Akkermansia muciniphila*, fracture healing, type H vessel, gut permeability, inflammation

© 2020. Published by The Company of Biologists Ltd.
This is an Open Access article distributed under the terms of the Creative Commons Attribution License (http://creativecommons.org/licenses/by/4.0), which permits unrestricted use, distribution and reproduction in any medium provided that the original work is properly attributed.

Disease Models & Mechanisms • DMM • Accepted manuscript

Summary statement

Akkermansia muciniphila promotes type H vessels formation and bone fracture healing by reducing inflammation.

ABSTRACT

Improving revascularization is one of the major measures in fracture treatment. Moderate local inflammation triggers angiogenesis, whereas systemic inflammation hampers angiogenesis. Previous studies showed that *Akkermansia muciniphila* (*A. muc*), a gut probiotic, ameliorates systemic inflammation by tightening intestinal barrier. In this study, fractured mice intragastrically administrated with *A. muc* were found to display better fracture healing than mice treated with vehicle. Notably, more preosteclasts positive for platelet-derived growth factor-BB (PDGF-BB) were induced by *A. muc* at 2 weeks post fracture, coinciding with increased formation of type H vessels, a specific vessel subtype that couples angiogenesis and osteogenesis and can be stimulated by PDGF-BB. Moreover, *A. muc* treatment significantly reduced gut permeability and inflammation at early stage. Dextran Sulfate Sodium (DSS) was used to disrupt the gut barrier to determine the role of gut barrier in fracture healing and whether *A. muc* still can stimulate bone fracture healing. As expected, *A. muc* evidently improved gut barrier, reduced inflammation, and restored the impaired bone healing and angiogenesis in DSS-treated mice. Our results suggest that *A. muc* reduces intestinal permeability and alleviates inflammation, which probably induces more PDGF-BB positive preosteoclasts and type H vessel formation in callus, thereby promoting fracture healing. This study provides the evidences about the involvement of type H vessels in fracture healing and suggests the potential of *A. muc* as a promising strategy for bone healing.

Disease Models & Mechanisms • DMM • Accepted manuscript

INTRODUCTION

With the rapid development of industry and transportation, the amount of bone fractures has remarkably increased in recent decades (Zhang et al., 2016). Although techniques of treatment and material of implantation have been constantly improved (Gu et al., 2012; Hayes and Richards, 2010; Wing-Hoi et al., 2011; Zhang et al., 2016), a part of patients with fractures still exhibit delayed healing or nonunion (Wang et al., 2016; Yuasa et al., 2015), which causes great medical and economic cost (Bhandari et al., 2017). Therefore, promoting fracture healing has become a worldwide challenge with great clinical and social significance.

An adequate blood supply is supposed to be a mediator for optimal fracture repair (Lim et al., 2017; Tomlinson et al., 2013). Due to the injury of vessels and vasoconstricition, blood flow evidently diminishes in the first few days post fracture (Claes et al., 2012). Around 2 weeks post fracture (WPF), blood supply of fracture site peaks and then gradually decreases to normal level (Claes et al., 2012; Lim et al., 2017). At early stage, a certain degree of inflammatory response is required to provoke angiogenesis cascade (Cottrell and O'Connor, 2010), whereas systemic or additional local inflammation can inhibit revascularization and impair fracture healing (Lim et al., 2017; Loi et al., 2016). Normally, damage of vessels and other soft tissue surrounding fracture zone induce local inflammation, which is considered as an initial cause of new blood vessels formation. However, previous studies showed that severe fracture or multiple traumatic fractures can increase intestinal permeability, causing bacterial translocation and systemic inflammation (Levy et al., 2006; Napolitano et al., 1996; Wrba et al., 2018). Restoring gut barrier has been demonstrated to improve several physical functions and ameliorate pathological changes, such as extending life span, sensitizing cancer to immune therapy and attenuating non-alcoholic steatohepatitis (Akagi et al., 2018; Bhutiani et al., 2018; Peng et al., 2018). Thus, we hypothesized that fracture induced systemic inflammation, at least to some extent, may hamper the bone repair. We also supposed that tightening intestinal barrier integrity may promote fracture healing by reducing inflammatory responses.

Previous studies showed that a specific vessel subtype named type H, featured by

Disease Models & Mechanisms • DMM • Accepted manuscript

highly expression of CD31 and Endomucin (Emcn), couples angiogenesis and osteogenesis (Kusumbe et al., 2014; Ramasamy et al., 2014). We previously proved that the preosteoclasts (POC), tartrate-resistant acid phosphatase–positive ($TRAP^+$) mononuclear cells, release platelet-derived growth factor-BB (PDGF-BB) to induce formation of this capillary subtype (Xie et al., 2014). Moreover, we and others revealed that pharmacological measures to increase type H vessels can obviously enhance the bone formation in both aged and ovariectomized mice (Huang et al., 2018; Kusumbe et al., 2014; Xie et al., 2014). An improved fracture healing also requires robust vessels formation (Claes et al., 2012). However, the evidence about the involvement of type H vessel during fracture healing process is still lacking.

In recent years, researchers have reached a consensus that the gut microbiota (GM) exerts profound effect on host`s health status (Gilbert et al., 2018). For skeletal system, a previous study showed that low dose of antibiotics treatment to mice at weaning shifts composition of GM and causes high bone mass (Cho et al., 2012). Supplementation of probiotics prevents sex steroid depletion-induced bone loss via maintaining gut barrier, inhibiting inflammation and suppressing osteoclastogenesis (Britton et al., 2014; Li et al., 2016b). *Akkermansia muciniphila* (*A. muc*) is a Gram-negative anaerobic commensal, accounting for 1%-5% of human GM (Derrien, 2004; Plovier et al., 2017). It has proved that this mucin-degrading microbe can thicken the mucosal layer and tighten the gut barrier (Derrien et al., 2017). Recently, its important role in intestinal ecosystem has been highly appreciated. Multiple studies indicated that *A. muc* has a wide range of biological activities, including ameliorating atherosclerotic lesions by attenuating lipopolysaccharide (LPS)-induced inflammation, preventing alcoholic liver disease through enhancing mucus thickness and tightening gut barrier, as well as improving metabolism in obese and diabetic mice (Grander et al., 2018; Li et al., 2016a; Plovier et al., 2017). Although accumulated evidences have illustrated the impacts of GM on bone and the benefits of *A. muc* to health, the effect of *A. muc* on bone fracture healing has not been reported. The effect of *A. muc* on intestinal epithelial barrier gives reason for studying whether it can mitigate fracture operation-induced gut permeability and systemic inflammation, and eventually

Disease Models & Mechanisms • DMM • Accepted manuscript

strengthen bone repair.

In this study, we assessed whether *A. muc* administration can promote fracture healing. We also tested the impact of this probiotic on PDGF-BB-releasing preosteoclasts and type H vessels. To find the possible reasons of pro-osteogenic and pro-angiogenic effects of *A. muc*, the inflammatory responses and gut permeability were detected. Besides, the impact of another probiotic on fracture healing was tested to investigate whether the fracture healing-promoting effect is specific to *A. muc*. We also used dextran Sulfate Sodium (DSS) to disrupt gut barrier to determine whether *A. muc* is still effective in promoting fracture healing. This study aimed to determine the therapeutic role of *A. muc* in bone repair and to explore the underlying mechanism preliminarily.

RESULTS

Mice treated with *A. muc* display improved quality of fracture healing

To study the impact of *A. muc* on fracture healing, we challenged specific pathogen free (SPF) 8-week-old female mice by osteotomy surgery and intramedullary implantation. All fractured mice were treated with either *A. muc* or the same volume of vehicle twice a week. Fecal samples were collected at 4 time points (1, 2, 4 and 6 WPF) and then all mice were sacrificed (Fig. 1A). For Characterization of *A. muc*, we extracted bacterial DNA of cultured *A. muc* for PCR amplification. Product of PCR was subjected to agarose gel electrophoresis with a DNA marker ranging from 100-600 base pairs (bps). The result showed DNA band appeared between 300 bps and 400 bps, which is consistent with fractional volume (329 bps) between forward primer and reverse primer in genomic DNA of *A. muc* (Fig. 1B). qRT-PCR analyses indicated that the *A. muc* abundance in faeces was significantly elevated by *A. muc* supplementation at 2, 4 and 6 WPF (Fig. 1C). These data indicated that the *A. muc* was successfully colonized in gut of mice.

To compare fracture healing quality of *A. muc* group and vehicle group, μCT analyses were performed to measure BV (mineralized bone volume in callus), TV (total callus volume) and BV/TV of callus (Zhang et al., 2016). At 1 WPF, μCT

Disease Models & Mechanisms • DMM • Accepted manuscript

results showed greater TV in *A. muc* group than that in vehicle group, but no significant difference of BV was found between two groups (Fig. 1D-F). At 4 and 6 WPF, the BV of *A. muc* group was much higher than that of vehicle group (Fig. 1E). The TV of both *A. muc*- and vehicle-treated mice peaked at 2 WPF and then gradually decreased, probably due to the callus remodeling (Fig. 1F). No statistical difference of TV was observed between the two groups since 2 WPF (Fig. 1F). The value of BV/TV in *A. muc* group was slightly lower at 1 WPF but obviously greater at 4 and 6 WPF, than that of vehicle group (Fig. 1G), which is attributed to the promoted BV of *A. muc* group at later stage. Tissue mineral density analysis shows that *A. muc* treatment enhanced callus mineralization at 6 WPF (Fig. 1H). Next, we performed four-point bending test at 6 WPF to test biomechanical properties of fractured femora. As shown in Fig. 1I, the maximum bending load of fractured femora in *A. muc* group was significantly greater than that in vehicle group. These results demonstrated that *A. muc* supplementation of a mouse femur fracture model resulted in more callus formation at early stage, and accelerated mineralization at later stage, as compared to vehicle treatment. We also performed 16S rDNA qRT-PCR analysis with a series of phylum- and class-specific primers (Bacchetti De Gregoris et al., 2011) to determine whether the *A. muc* supplementation altered the gut microbiome. As shown in Fig. S1A, *A. muc* induced a marked increase of Actinobacteria, which consistent with previous study (Wu et al., 2020). In addition, *A. muc* colonization reduced abundance of γ-Proteobacteria and led to a trend of increase of Bacteroidetes.

To confirm the direct effect of *A. muc* exerted on fracture healing, an antibiotics (ABX) cocktail (vancomycin, ampicillin, neomycin and metronidazole) was used to deplete the gut microbiota (Blacher et al., 2019). Then mice were fractured and the effect of *A. muc* was re-tested. As shown in Fig. S1B-F, *A. muc* still promoted bone fracture healing in ABX-treated mice. Both BV and TV were elevated at the 6 WPF, resulting to an improved anti-bending property (Fig. S1B-F). qRT-PCR analyses showed that the *A. muc* was successfully colonized in gut of ABX-treated mice (Fig. S1G). Our results suggested that *A. muc* has the ability to stimulate fracture repair through an endogenous microbiota-independent mechanism.

Disease Models & Mechanisms • DMM • Accepted manuscript

Mice treated with *A. muc* display improved bone formation

We then asked whether *A. muc* treatment influenced chondroid callus formation, bone formation and bone resorption. Safranin O staining at 2 WPF showed more chondroid matrix was formed in fracture callus of *A. muc*-treated mice, as compared to vehicle-treated mice (Fig. 2A-B), which is thought to benefit endochrondral ossification at later stage. Consistently, immunostaining of osteocalcin showed more osteoblasts (the cells responsible for bone formation) in callus area at 6 WPF in *A. muc* group, as compared with vehicle group (Fig. 2C-D). ELISA results showed that the serum level of osteocalcin (OCN, serum marker of bone formation) was also significantly elevated by *A. muc* treatment (Fig. 2E). TRAP staining indicated that the difference of $TRAP^+$ multinucleated cells (osteoclasts, the cells responsible for bone resorption) was not statistically significant between two groups at 6 WPF (Fig. 2F-G). Consistently, no obvious difference of C-terminal telopeptides of type 1 collagen in serum (CTX-1, serum marker of bone resorption) between two groups could be detected (Fig. 2H). These data illustrated that supplementation of *A. muc* improved fracture healing at both early and later stages, and the better bone repair may attribute to increased bone formation.

***A. muc* treatment stimulates type H vessel formation in callus**

Type H vessels are responsible for supporting bone formation (Huang et al., 2018; Ramasamy et al., 2014; Xie et al., 2014). Our previous study showed that preosteoclasts could release PDGF-BB to induce formation of type H vessel for attenuating bone loss in sex steroid deficient mice (Xie et al., 2014). However, the involvement of type H vessels in fracture repair has not been reported. We then investigated whether *A. muc* treatment could stimulate type H vessel formation during fracture healing.

Since vessel formation in fracture zone reaches high level at about 2 WPF (Lim et al., 2017), we verified the number of preosteoclast and osteoclast at this time point. TRAP staining showed distinct more preosteoclasts and less osteoclasts on the surface

Disease Models & Mechanisms • DMM • Accepted manuscript

of woven bone in *A. muc*-treated mice at 2 WPF, as compared to vehicle-treated mice (Fig. 3A-B). We previously reported preosteoclasts stimulate type H vessel formation by secreting PDGF-BB. Therefore, coimmunostaining of TRAP and PDGF-BB at 2 WFP was conducted. As expected, more preosteoclasts ($TRAP^+$ mononuclear cells) positive for PDGF-BB were detected on the surface of woven bone in fracture area of *A. muc*-treated mice than that of vehicle-treated mice (Fig. 3C-D). Next, to determine the formation of type H vessel, coimmunostaining of CD31 and Emcn was performed at 2 WPF. The data showed that the formations of both total vessel and type H vessel were significantly higher in fracture area of *A. muc*-treated mice as compared to vehicle-treated mice, whereas the formation of none-type H vessel was similar between the of two groups (Fig. 3E-H). Taken together, *A. muc* treatment effectively boosted type H vessel formation in callus, which was probably attributed to increased number of $PDGF\text{-}BB^+$ preosteoclasts in fracture area.

A. muc administrated mice exhibit lower level of inflammatory responses at early stage of fracture healing

Excessive inflammation is considered as one of the most important systemic factors that inhibit blood vessel formation during fracture healing (Claes et al., 2012; Schmidt-Bleek et al., 2015). Previous reports, including ours, have demonstrated that excessive inflammation stimulates preosteoclast fusion, thus promoting bone resorption (Li et al., 2016b; Rao et al., 2018). Given to the anti-inflammatory effects of *A. muc in vivo* (Grander et al., 2018; Li et al., 2016a), we measured local inflammation level of fracture site at 2 WPF. Immunohistochemical analyses showed weaker staining intensities of interleukin-1β (IL-1β), IL-6 and tumor necrosis factor-α (TNF-α) in fracture area of *A. muc* group than that of vehicle group (Fig. 4A-F). Notably, all these pro-inflammatory cytokines we tested were proved to impair angiogenesis in fracture healing (Chambers et al., 2018; Kaiser et al., 2018; Lange et al., 2010; Lim et al., 2017; Prystaz et al., 2018).

Macrophage colony-stimulating factor (M-CSF, also called CSF1) is required by preosteoclasts survival, proliferation and osteoclastic differentiation, while the

Disease Models & Mechanisms • DMM • Accepted manuscript

receptor activator of nuclear factor-kappaB ligand (RANKL), another key osteoclastogenesis cytokine, is responsible for osteoclasts formation and activation of osteoclastic resorptive function (Kong et al., 2020). Then we evaluated the level of M-CSF and RANKL in serum. Fig. S2A-B showed that both two factors were obviously downregulated by *A. muc* at 2 WPF, during which the *A. muc* exerted anti-inflammatory effect on fracture site. Consistent with our results, multiple previous studies demonstrated that inflammation can stimulate production of M-CSF and RANKL (Meng et al., 2020; Mossadegh-Keller et al., 2013; Pietschmann et al., 2016). RANKL alone can`t induce osteoclastogenisis without M-CSF (Seo et al., 2007). These data, when taken together, suggest that the anti-inflammatory outcome of *A. muc* treatment may be the reason of more preosteoclasts and type H vessels, as well as the accelerated fracture healing.

***A. muc* treatment decreases intestinal permeability and inflammation**

Previous studies showed that the anti-inflammatory effects of *A. muc* are largely correlated to restoration of the gut barrier function, rendering a correction of bacterial LPS under some pathological circumstances (Grander et al., 2018; Li et al., 2016a; Plovier et al., 2017). Since fracture was proved to increase gut permeability, we analyzed intestinal mRNA expression of a class of the tight junction proteins, including occludin, jam-3, claudin-2, -3, and -15 (Li et al., 2016b; Plovier et al., 2017). Fig. 5A-E showed that intestinal mRNA levels of these factors were significantly higher in *A. muc*-treated mice as compared to vehicle-treated mice at 2 WPF. To further confirm the improved gut barrier induced by *A. muc*, mice in two groups were administrated orally with fluorescein isothiocyanate–dextran (FITC-dextran) at 2 and 6 WPF. 4 hours later, serum concentrations of FITC-dextran were tested. As shown in Fig. 5F, vehicle-treated mice had much higher serum level of FITC-dextran at 2 WPF, whereas the difference between two groups at 6 WPF was not significant. LAL assay indicated that *A. muc* treatment led to decreased circulatory LPS than vehicle treatment at 2 WPF but not 6 WPF (Fig. 5G). Correspondingly, as compared to vehicle-treated mice, *A. muc*-treated mice exhibited significantly lower intestinal

Disease Models & Mechanisms • DMM • Accepted manuscript

mRNA levels of pro-inflammatory factors TNF-α and IL-17a, but significantly higher intestinal mRNA level of anti-inflammatory factor IL-10 at 2 WPF (Fig. 5H-J). The gut barrier tightening effect and intestinal anti-inflammatory effect of *A. muc* at 6 WPF were not as strong as that at 2 WPF (Fig. 5A-J). To test the effect of *A. muc* on systemic inflammation, serum samples were tested by ELISA. The results suggested that at early stage *A. muc* evidently elevated level of anti-inflammatory factor IL-10 and reduced the level of TNF-α and serum amyloid A3 (SAA3) (Fig. 5K-M), two factors thought to promote inflammation and to stimulate osteoclastogenesis (Thaler et al., 2015; Thompson et al., 2018). Taken together, these data suggest *A. muc* treatment evidently reduced gut permeability and systemic inflammation at early stage, during which the angiogenesis of fractured area reaches the highest level (Lim et al., 2017).

Supplementation of probiotics promote bone fracture healing

We then asked whether the improved fracture healing is specific to *A. muc* and whether other probiotics that reduce gut permeability and inflammation could also promote bone repair. *Lactobacillus gasseri* (*L. gas*) was reported to ameliorate inflammation and obesity, tighten gut barrier integrity, and improve glucose tolerance (Kawano et al., 2016; Shirouchi et al., 2016). Then we re-evaluated impact of *A. muc* on fracture healing, with one additional control group of *L. gas* treatment. μCT scanning showed that mice received with *L. gas* treatment exhibited higher BV at 2 WPF and higher TV at 6 WPF, as compare with vehicle treated mice (Fig. 6A-D). Biomechanical test also showed that the femora of *L. gas*–treated mice had better healing quality than that of vehicle-treated mice (Fig. 6E). Safranin O staining at 2 WPF showed that chondroid matrix formation in fracture callus was slightly increased by *L. gas* (Fig. 6F,G). We also found that *L. gas* treatment lead to more preosteoclasts in callus at 2 WPF (Fig. 6H,I). Similar to the *A. muc*, *L. gas* treatment promote formation of new vessels, especially that of type H vessel (Fig. 6J,K). These results suggest that *L. gas* treatment also has ability to improve the bone fracture healing.

Disease Models & Mechanisms • DMM • Accepted manuscript

A. muc treatment rescued gut barrier dysfunction-induced impairment of bone healing

To understand the role of gut barrier in fracture repair and whether *A. muc* is still effective when intestinal permeability increases, dextran sodium sulfate (DSS) was employed to disrupt intestinal barrier. All the mice were divided into 3 groups: vehicle group, DSS + vehicle group and DSS + *A. muc* group. Before surgery and *A. muc* administration, a 7-day DSS treatment (2.5% w/v) was given to DSS + vehicle group and DSS + *A. muc* group. After surgery, 3 rounds of DSS treatment (8-day normal drinking water followed by 6-day DSS) were performed. Mice in vehicle group only drank normal water. As shown in Fig. 7A, all the mice received DSS exhibited obvious low body weight at early stage. However, by the day 35, mice in DSS + *A. muc* group began to gain higher body weight than DSS + vehicle group mice. At late stage of experiment, mice in DSS + *A. muc* group showed similar body weight with vehicle group (Fig. 7A). Colon lengths showed that DSS treatment significantly shortened colon while *A. muc* treatment significantly alleviated the intestinal damage (Fig. 7B,C). Hematoxylin eosin (HE) staining of colonic sections showed that *A. muc* treatment distinctly rescued the mucosal damage and intestinal inflammation induced by DSS, at both 2 and 6 WPF (Fig. 7D,E).

μCT results show that DSS hampered bone healing, as indicated by less BV and TV at both 2 and 6 WPF (Fig. 7F,G). DSS + *A. muc* group mice exhibited much higher BV and TV than that of DSS + vehicle group mice, and even mild higher BV/TV than vehicle group mice at 6 WPF (Fig. 7F-H). Four-point bending test suggested that *A. muc* obviously enhanced biomechanical properties in DSS-treated mice (Fig. 7I). Additionally, *A. muc* treatment restored chondroid matrix formation and number of preosteoclast, as evidenced by safranin O staining and TRAP staining (Fig. 7J-M).

We also tested the angiogenesis of three groups. As shown in Fig. 8A-D, DSS treatment significantly reduced new vessel formation, including the type H vessel and non-type H vessels. *A. muc* treatment attenuated the loss of angiogenesis caused by DSS, largely due to the type H vessel (Fig. 8A-D). Next, a class of gut barrier and inflammation-related mRNA were tested. The data demonstrated that *A. muc*

Disease Models & Mechanisms • DMM • Accepted manuscript

treatment can tighten impaired gut barrier integrity and decrease colonic inflammation in DSS-treated mice (Fig. 8E-L). Consistently, the serum LPS level and serum FITC-dextran level also indicate that *A. muc* treatment reduced intestinal permeability (Fig. 8M,N). These evidences, when taken together, suggest that *A. muc* treatment can promote bone repair and type H vessels formation via tightening gut barrier and deceasing inflammation.

DISCUSSION

Recent advances in how gut microbiota contribute to host`s physiological and pathological states have generated great attention on employing probiotics to improve human health. Probiotics have been identified as "live microorganisms, which upon ingestion in certain numbers, exert health benefits beyond inherent basic nutrition" (Guarner and Schaafsma, 1998). Several probiotics have shown their bone-sparing effects, such as anti-osteoporosis and enhancing bone mass (Li et al., 2016b; Ohlsson et al., 2014). However, the effect of probiotics on fracture healing is less well studied. Over the past few years, *A. muc* has been introduced as a next-generation probiotic because of its positive bioactivities on host health (Naito et al., 2018), especially the anti-inflammatory effect. Previous studies have demonstrated that supplementation of *A. muc* can ameliorate several inflammation-related diseases by enhancing colonic mucus thickness and tightening gut barrier (Grander et al., 2018; Li et al., 2016a; van der Lugt et al., 2019). In this study, we showed that *A. muc* supplementation improves bone fracture healing in both normal SPF mice and gut microbiota-depleted mice, which provide a new approach for bone-related disease treatment and broaden the potential clinical application of *A. muc*.

The process of fracture repair contains three partially overlapping periods: inflammation, repair and remodeling (Claes et al., 2012). Once fracture happened, fracture hematoma is gradually formed, caused by bone-surrounding soft tissue injury and hemorrhage (Paula et al., 2010; Richard and Einhorn, 2011). Injuries-initiated inflammation is thought positive to angiogenesis and fracture repair when it is moderate (Loi et al., 2016). However, previous studies reported that bone fracture

Disease Models & Mechanisms • DMM • Accepted manuscript

weaken gut barrier integrity, leading to bacterial translocation-caused systemic inflammation (Levy et al., 2006; Napolitano et al., 1996; Wrba et al., 2018). In our present study, we firstly applied *A. muc* to treat fractured mice, and found that fractured mice administrated with *A. muc* display improved gut epithelial barrier integrity and reduced inflammatory responses. Previous studies showed that *A. muc* and *A. muc*-derived extracellular vesicles (EVs) can alleviate DSS-induced colitis (Chelakkot et al., 2018; Kang et al., 2013; Zhai et al., 2019), which is characterized by mucosal damage and inflammation infiltration. In our study, *A. muc* significantly preserve the gut barrier and restore the loss of endochondral ossification and angiogenesis induced by DSS. Consistently, *A. muc* treatment caused less osteoclasts in fracture area at 2 WPF, in agreement with previous results that osteoclasts generation is augmented in inflammatory condition and inhibiting inflammation can prevent osteoclastogenesis (Li et al., 2016b; Rao et al., 2018). Our data suggested that tightened gut barrier is of great importance for fracture healing, which provide potential explanation and therapeutic tool for delayed union and nonunion. We also found *L. gas*, another probiotic that has also been proved to reduce intestinal permeability and inflammation, exert pro-angiogenesis effect and promote bone healing, implying that not only *A. muc*, but also other probiotics can benefit bone repair. Notably, *L. gas* shows a trend of decreased fracture healing-promoting effect, as compared to *A. muc*.

The importance of angiogenesis in fracture healing has long been highly appreciated. Previous studies demonstrated that the type H vessel couples angiogenesis and osteogenesis, and mediates local growth of vasculature (Kusumbe et al., 2014; Ramasamy et al., 2014). We previously proved that preosteoclasts-released PDGF-BB could stimulate type H vessel formation and drugs increasing preosteoclasts could promote bone formation in estrogen deficient mice (Huang et al., 2018; Xie et al., 2014; Yin et al., 2018). In another study, drug promote type H vessel formation in subchondral bone has been prove to attenuates osteoarthritis progression (Cui et al., 2016). In this study, we firstly observed the existence of type H vessels in callus and found that *A. muc* stimulates generation of this vessel subtype, which may

Disease Models & Mechanisms • DMM • Accepted manuscript

be associated with the anti-inflammatory effect of *A. muc* and the reason of better fracture repair of *A. muc* treatment. We also found the increase of angiogenesis induced by *A. muc* was mainly attributed to the type H vessels formation, which highlighted the importance of type H vessels to fracture healing. PDGF-BB, which was proved to benefit vessels formation and fracture healing (Walia et al., 2018), was also detected in callus of *A. muc*-treated mice. These data suggest that increased number of PDGF-BB^{+} preosteoclasts induced by *A. muc* might stimulate CD31^{hi}Emcn^{hi} vessels formation in callus. Considering the involvement of type H vessels in bone healing, drugs that improve this specific capillary subtype or inhibit osteoclastogenesis (Huang et al., 2018; Yin et al., 2018) have potential to improve fracture.

There are some limitations in our study. The difference of *A. muc* abundances at 1 WPF between *A. muc*–treated mice and vehicle-treated mice was not significant enough, while the obvious increase of *A. muc* abundance in mice feces appeared at 2 WPF. We hypothesized that many of the exogenously administered *A. muc* may be eliminated from the mice body during the washout period (van der Lugt et al., 2019) and two times of colonization may be not sufficient to provide enough *A. muc* that can survive and grow in the host gut. On the other hand, it may be also possible that the transplantation of *A. muc* alters the endogenous microbiota and preferentially enables the endogenous *A. muc* to outcompete other bacteria, thus increasing the abundance of *A. muc* in the mice gut with 2 weeks. Besides, the role of PDGF-BB^{+} preosteoclasts in *A. muc*-boosted type H vessel formation has not been determined. This warrants further studies.

To sum up, we show that *A. muc* improves type H vessel formation and bone repair which may associated with its effects in tightening the intestinal barrier and decreasing systemic inflammation, at the early stage of fracture healing. Our study suggests that the *A. muc* can be applied as a therapeutic agent for promoting fracture healing.

Disease Models & Mechanisms • DMM • Accepted manuscript

MATERIALS AND METHODS

Culture and characterization of *A. muc*

We cultured *A. muc* (ATCC BAA-835, USA) anaerobically at 37 ℃ with constant shaking (135 rpm) in brain-heart-infusion (BHI) broth containing 0.05% L-cysteine-HCl (Sigma-Aldrich, USA) and 0.5% porcine mucin (Sigma-Aldrich) in accordance with manufacturer's instruction and previous reports (Li et al., 2016a; Shen et al., 2017). Concentration of *A. muc* was assessed by measuring the absorbance at the wavelength of 600 nm (Li et al., 2016a).

To characterize above mentioned *A. muc*, centrifugation (8,000 × g, 10 min, 4 ℃) was performed to collect bacterial pellet. Total genomic DNA was obtained with a TIANamp Bacteria DNA Kit (Tiangen, DP302, China). Polymerase chain reaction (PCR) amplification product of *A. muc* DNA was subjected to agarose gel electrophoresis and then ChemiDoc XRS+ system (Bio-Rad, USA) was used for DNA band imaging.

Animals and treatments

Animal care and experimental procedures were approved by the Ethical Review Board at Xiangya Hospital of Central South University. All the animal experiments were conducted in Department of Laboratory Animals, Central South University. 8-week-old C57BL/6 female mice were used for surgical fracture and implantation, as described previously (Yuasa et al., 2015; Zhang et al., 2016). After general anaesthesia by sodium pentobarbital intraperitoneal injection (50 mg/kg), an incision from mid femur to knee was made at the lateral right hindlimb of mouse, and blunt dissection of muscle was performed to expose mid-shaft of femur. A sterilized 23-gauge (about 0.64 mm outer diameter) needle was drilled into intercondylar notch of distal femur. In bone marrow cavity, needle was inserted along the axis of femoral shaft until it penetrated through proximal femur. A transverse fracture was made in the mid-shaft of femur using sharp scissors. After we confirmed that the fracture was complete, the wound was sutured. For *A. muc* group and *L. gas* (ATCC 33323) group,

Disease Models & Mechanisms • DMM • Accepted manuscript

each mouse was orally administrated with 8×10^8 cfu *A. muc* or *L. gas* in 0.5 mL PBS. Equivalent volume of PBS was given to each mouse of vehicle group. These treatments were conducted twice a week. Mice were sacrificed under general anaesthesia at 1, 2, 4 and 6 WPF. Whole-blood samples were collected by eyeball enucleation, and centrifugation (1,000 × g, 4 ℃, 15 min) was performed to obtain serum samples, which were stored at −80 °C before analysis.

For ABX treatment, mice were divided into 2 groups: ABX + vehicle and ABX + *A. muc* group. All mice were given a cocktail of broad-spectrum antibiotics with vancomycin (0.5 g/L, Macklin, China), ampicillin (1 g/L, Macklin, China), neomycin (1 g/L, Macklin, China) and metronidazole (1 g/L, Macklin, China) in drinking water for 2 weeks, followed by 2 days of washout period (Blacher et al., 2019). Fecal samples were subjected to YCFA (1 g casitone, 0.25 g yeast extract, 0.4 g NaHCO3, 0.1 g cysteine, 0.045 g K2HPO4, 0.045 g KH2PO4, 0.09 g NaCl, 0.009 g MgSO4•7H2O, 0.009 g CaCl2, 0.1 mg resazurin, 1 mg haemin, 1 µg biotin, 1 µg cobalamin, 3 µg p-aminobenzoic acid, 5 µg folic acid, 15 µg pyridoxamine, 0.2g glucose, 0.2g maltose and 0.2g cellobiose, per 100 mL) agar plates (Browne et al., 2016) with 96 hours anaerobic culturing to ensure fecal microbiota depletion. Then all the mice were conducted fracture surgery. Since previous study (Derrien et al., 2017; Geerlings et al., 2018) showed that *A. muc* was found to resist vancomycin and metronidazole, combination of vancomycin (0.5 g/L) and metronidazole (1 g/L) was given to all the mice until end of experiment to prevent the re-colonization of environmental bacteria. For ABX + *A. muc* group mice, *A. muc* treatment started at the day of surgery. 8×10^8 cfu *A. muc* in 0.5 mL PBS was given by oral gavage to each mouse in ABX + *A. muc* group and same volume of PBS was given to mice in ABX + vehicle group, twice a week, for a total of 6 weeks.

In DSS experiment, all the mice were divided into 3 groups: vehicle group, DSS + vehicle group and DSS + *A. muc* group. For mice in DSS + vehicle group and DSS + *A. muc* group, 2.5% (w/v) DSS (40 KDa, Sigma-Aldrich, 52423) was added into drinking water *ad libitum*. A 7-day DSS treatment was given to DSS + vehicle group

Disease Models & Mechanisms • DMM • Accepted manuscript

and DSS + *A. muc* group before fracture operation. After surgery, 3 cycles of treatment (8-day normal drinking water followed by 6-day DSS) were performed until the experimental end point (Chen et al., 2020; Liu et al., 2019). Mice in vehicle group received normal drinking water during the whole experiment. 8×10^8 cfu *A. muc* in 0.5 mL PBS was orally administrated to each mouse in DSS + *A. muc* group twice a week. Equivalent volume of PBS was given to each mouse of vehicle group and DSS + vehicle group. All the mice were weighed twice a week until sacrificed.

Quantification of *A. muc* in faeces and 16S rDNA qRT-PCR analysis

Fecal genomic DNA was extracted with a TIANamp stool DNA kit (Tiangen, DP328). Quantitative real-time PCR (qRT-PCR) was carried out to amplify the specific *A. muc* gene sequence with a pair of specific primers (forward 5′-CCTTGCGGTTGGCTTCAGAT-3′ and reverse 3′-CAGCACGTGAAGGTGGGGAC-5′) (Grander et al., 2018) by using FastStart Universal SYBR Premix ExTaq (Takara Biotechnology, Japan) (Chen et al., 2018; Hu et al., 2018). Cycle threshold (CT) value of each sample was then compared with a standard curve made by diluting genomic DNA of *A. muc*. Log_{10} of *A. muc* number per gram of fecal content was used to indicate the abundance of *A. muc* (Grander et al., 2018; Li et al., 2016a).

16S rDNA qRT-PCR analysis was performed as previously described (Bacchetti De Gregoris et al., 2011). Briefly, a fecal DNA sample was diluted 1:4. These two samples (undiluted sample and diluted sample) were subjected to qRT-PCR for testing the amplification efficiency of each primer pair (Fig. S2) with following formulas:

$$\text{a: } N = N_0 \times (Eff)^{Ct1}$$

$$\text{b: } N = \frac{1}{4} \times N_0 \times (Eff)^{Ct2}$$

Here N is a constant which refers to threshold of qRT-PCR and N_0 refers to original DNA content of template. Eff is amplification efficiency. Ct1 and Ct2 represent cycle threshold (Ct) value of undiluted sample and diluted sample, respectively. Eff of each primer pair can be calculated by formula below (formula a/formula b):

Disease Models & Mechanisms • DMM • Accepted manuscript

$$(\text{Eff})^{\text{Ct1-Ct2}} = \frac{1}{4}$$

Percentage of each taxonomic group in feces (X) was calculated by Ct value and amplification efficiency of each primer pair with the formula:

$$X = (\text{Eff. Univ})^{\text{Ct. Univ}}/(\text{Eff. Spec})^{\text{Ct. Spec}} \times 100\%$$

Eff. Univ and Eff. Spec represent amplification efficiency of universal primers and taxon-specific primers. Ct. Univ and Ct. Spec represent Ct value of universal primers and taxon-specific primers. Primers used for 16S rDNA qRT-PCR are listed in Table. S1.

Micro computed tomography (μCT) analyses

Fractured femora harvested from mice were fixed overnight in 4% paraformaldehyde and analyzed by μCT (SCANCO Medical AG, vivaCT 80; Switzerland) as described in our previous studies (Huang et al., 2018; Rao et al., 2018). The scanner was set at voltage of 55 kV, current of 145 μA and voxelsize of 11.4 μm, respectively. 600 slices were analyzed and fracture line was set in middle of this range. The region of interest (ROI) was selected slice-by-slice and a fixed threshold (≥60) was used to define mineralized tissue in callus. Total callus volume (TV), mineralized bone volume in callus (BV) and BV/TV of callus were calculated.

Biomechanical test

After μCT scanning, four-point bending test was performed to test the fracture-healing quality of femora using a computer-controlled mechanical testing machine (Instron, 3343M1372, USA) (Zhang et al., 2016). In brief, femora were placed in the anterior–posterior direction (patella side facing up) on the lower supporting bars at 9 mm apart. Upper bars span measured 5.5 mm. A constant vertical compression load was applied at speed of 3 mm/min until failure happened. The values of maximum bending load (N) were recorded automatically by computer.

Disease Models & Mechanisms • DMM • Accepted manuscript

Histological, immunohistochemical, and immunofluorescent analyses

For the histological and immunohistochemical staining, dissected femora were fixed in 4% paraformaldehyde overnight and decalcified in 0.5 M EDTA (pH = 7.4) at 4 ℃ with constant shaking for about 3 days. After that, dehydration was performed with a graded series of ethanol, following with paraffin embedding. Bone samples were sliced longitudinally at a thickness of 5 μm and processed for TRAP staining (Sigma-Aldrich, 387A) to measure osteoclasts formation in accordance with our established protocols (Huang et al., 2018; Rao et al., 2018). $TRAP^+$ mononuclear cells were defined as preosteoclasts and $TRAP^+$ multinucleated cells (at least three nuclei) were identified as osteoclasts.

The level of inflammatory responses in bone tissues were tested by IL-1β, IL-6 and TNF-α immunohistochemical analyses as we previously reported (Rao et al., 2018). Antibodies against IL-1β (16806-1-AP, 1:50), IL-6 (21865-1-AP, 1:200) and TNF-α (17590-1-AP, 1:100) were obtained from ProteinTech (USA) and the secondary antibodies were purchased from Abcam (ab150088, 1:200).

For safranin O staining (Yuasa et al., 2015), deparaffinization and rehydration were performed as usual. Sections were placed in hematoxylin for 2 min and washed in running tap water for 5 min. After 0.1% safranin O (Sigma-Aldrich, S2255) staining for 3 min and 1% acetic acid rinsing for 10-15 seconds, sections were stained with 0.1% fast green solution (Sigma-Aldrich, F7258) for 5 min, following with running tap water washing for 5 min. Finally, dehydrated sections were coverslipped with Permount and images were acquired with an optical microscope (Olympus, CX31, Germany).

For analysis of colonic damage induced by DSS, colon samples were fixed in 4% paraformaldehyde at 4 ℃ overnight. After PBS rinsed for 3 times, dehydration and paraffin embedding were performed as described above. Colon samples were sectioned transversely at a thickness of 5 μm and processed for HE staining. Scoring was conducted as described previously (Welz et al., 2011). In brief, we added scores of inflammation and tissue damage on different levels from 0 to 3, from which the

Disease Models & Mechanisms • DMM • Accepted manuscript

total colon histological scores of 0 to 6 were obtained. Inflammation score was defined as: 0, no inflammatory infiltration detected in lamina propria; 1, presence of inflammatory cells in mucosa; 2, inflammatory infiltration in submucosa; 3, transmural inflammatory infiltration. Tissue damage score was defined as: 0, no mucosal damage; 1, discrete lesions in colonic epithelium; 2, extended epithelial damage detected in elongated crypts-containing areas, crypt abscesses or focal ulceration; 3, extended ulceration in colonic wall.

Image-Pro Plus software (version 6.0) was employed to measure staining intensity and positive-stained cells or area in quantitative analyses of histological, immunohistochemical staining.

For all immunofluorescent staining, femora were fixed in 4% paraformaldehyde for 4 hours and decalcified in 0.5 M EDTA (pH = 7.4) at 4 ℃ with constant shaking for about 2-3 days. Bone samples were immersed in 30% sucrose overnight for dehydration. After exposure to liquid nitrogen for a few seconds, samples were embedded in optimal cutting temperature (OCT) compound (Sakura Finetek, USA) and sectioned at corresponding thickness of each assay. 5-μm-thick sections were incubated with osteocalcin (OCN) antibody (1:200, Abcam, ab93876) overnight at 4 ℃. Then, the secondary antibody Cy™3 AffiniPure Goat Anti-Rabbit IgG (H+L) (Jackson ImmunoResearch, 111-165-003, 1:300) was incubated at room temperature for 1 hour while protected from light. Slices of 10-μm thickness were stained with TRAP antibody (Santa Cruz, sc-30833, 1:200) and PDGF-BB antibody (Abcam, ab21234, 1:50), as well as the corresponding secondary antibodies Donkey Anti-Goat IgG H&L (Alexa Fluor® 488) (Abcam, ab150129, 1:300) and Cy™3 AffiniPure Goat Anti-Rabbit IgG (H+L) (Jackson ImmunoResearch, 111-165-003, 1:300). For type H vessels immunofluorescent staining (Ramasamy et al., 2014), samples were cut into 30 μm thick. Primary antibodies to CD31 (Abcam, ab28364, 1:50) and Emcn (Santa Cruz, V.7C7, 1:100), Cy™3 AffiniPure Goat Anti-Rabbit IgG (H+L) (Jackson ImmunoResearch, 111-165-003, 1:300) and Alexa Fluor® 488 AffiniPure Donkey Anti-Rat IgG (H+L) (Jackson ImmunoResearch, 712-545-150, 1:300) were applied. Sections were observed with a fluorescence microscope (Carl Zeiss, Axio Imager 2,

Disease Models & Mechanisms • DMM • Accepted manuscript

Germany). The total vessel area (TVA; positive for Emcn), callus area (CA), type H vessel area (HVA; positive for Emcn and CD31) and none-type H vessel area (NHA; positive for Emcn and negative for CD31) were measured by Image-Pro Plus software (version 6.0) and Image J software (version 1.51) to calculate TVA/CA, HVA/TVA and NHA/CA (Huang et al., 2018).

The numbers of positive stained cells and relative staining intensity were determined in three sections per mouse and three mice per group.

qRT-PCR analyses

Colonic RNA was extracted with TRIzol Reagent (Invitrogen, USA) and RevertAid First Strand cDNA Synthesis kit (Fermentas, Canada) was used to synthesize cDNA. After that, FastStart Universal SYBR Premix ExTaqTM II (Takara Biotechnology) on an ABI PRISM® 7900HT System (Applied Biosystems, USA) was employed to conduct qRT-PCR. Relative gene expressions were measured by the $2^{-\Delta\Delta CT}$ method with the reference of GAPDH. qRT-PCR primers used in this study were as follows (Li et al., 2016b; Morhardt et al., 2019; Plovier et al., 2017): for *Cldn2*, 5′-TCTCAGCCCTGTTTTCTTTGG-3′ (forward) and 5′-GGCGAGCAGGAAAAGCAA-3′ (reverse); for *Cldn3*, 5′-TCATCACGGCGCAGATCA-3′ (forward) and 5′-CTCTGCACCACGCAGTTCA-3′(reverse); for *Cldn15*, 5′-GGCGGCATCTGTGTCTTCTC-3′ (forward) and 5′-TGGTGGCTGGTTCCTCCTT-3′ (reverse); for *Ocln*, 5′-ATGTCCGGCCGATGCTCTC-3′ (forward) and 5′-TTTGGCTGCTCTTGGGTCTGTAG-3′(reverse); for *Jam3*, 5′-CACTACAGCTGGTACCGCAATG-3′ (forward) and 5′-CTGGGATTGGCTCTGGAATC-3′ (reverse); for *Rankl*, 5′-CCTGATGAAAGGAGGGAGCA-3′ (forward) and 5′-TGGAATTCAGAATTGCCCGA-3′(reverse); for *Tnfα*, 5′-AACTCCAGGCGGTGCCTAT-3′ (forward) and 5′-TGCCACAAGCAGGAATGAGA-3′ (reverse); for *Il-10*,

Disease Models & Mechanisms • DMM • Accepted manuscript

5′-CCCTTTGCTATGGTGTCCTT -3′ (forward) and 5′-TGGTTTCTCTTCCCAAGACC -3′ (reverse); for *Il17a*, 5′-TGACGCCCACCTACAACATC-3′ (forward) and 5′-CATCATGCAGTTCCGTCAGC-3′(reverse); for *Gapdh*, 5′-CACCATGGAGAAGGCCGGGG-3′ (forward) and 5′-GACGGACACATTGGGGGTAG-3′(reverse).

Gut permeability assays

We used FITC-dextran (Sigma-Aldrich, FD4) to assess barrier function by oral administration as described previously (Li et al., 2016b). Briefly, each mouse was given 0.5 mL of 25 mg/mL FITC-dextran and serum samples were collected 4 hours later under general anaesthesia. The serum dextran level was determined by comparing with standard curve, which was developed by serial dilutions of known concentration of FITC-dextran using a spectrophotometer (Varioskan ™ LUX, Thermo Scientific) with excitation at 490 nm and emission at 520 nm. To quantify the LPS level in serum of mice, a LAL assay kit purchased from GeneScript (USA) was used in accordance with manufacture`s instruction.

Enzyme-linked immunosorbent assay (ELISA)

The concentrations of serum TNF-α, IL-10 and M-CSF were evaluated by using commercial ELISA kits (Multisciences Biotech, China). Serum RANKL, OCN and CTX-1 level were tested with ELISA kits purchased from Elabscience (China). Another ELISA kit (Cusabio, China) was applied to measure the level of SAA3. All the procedures were conducted according to the manufacturer`s instruction.

Statistical analyses

All data were presented as mean ± SD. Unpaired two tailed Student's *t* test was used to analyze the differences between two groups. One-way or two-way ANOVA with Bonferroni *post hoc* test was used for multiple-group comparisons. For all experiments, $P < 0.05$ was considered to be significant. GraphPad Prism software (Version 6.01) was used for above statistical analyses.

Disease Models & Mechanisms • DMM • Accepted manuscript

Acknowledgments

We thank Prof. Fei Yang and Fei-Yu Huang for their assistance in the bacterial propagation. We also thank Prof. Chun-Yuan Chen for the assistance in manuscript preparation.

Competing interests

The authors declare no competing or financial interests.

Author contributions

HX and JHL conceived the study and drafted the manuscript. RX and YZ conceived the study. JHL performed main part of the experiments, analyzed the data and prepared all the figures. TY maintained mice, harvested tissue samples, performed qRT-PCR assays, and helped with bacterial culturing and animal experiments. ZWL helped with bacterial culturing and conducted agarose gel electrophoresis. LJ and TFW helped with the histological, immunohistochemical, and immunofluorescent experiments. JC, ZQY, ZGW and CJS provided suggestions and technical support. All authors reviewed and approved the manuscript.

Funding

This work was supported by the National Natural Science Foundation of China (81670807, 81871822, 81522012, 81600699); Thousand Youth Talents Plan of China (D1119003); Medicine and Health Science and Technology Innovation Project of Chinese Academy of Medical Sciences (2019-RC-HL-024); High Level Talent Gathering Project of Hunan Province (2017XK2039); Innovation Driven Project of Central South University, China (2016CX028, 2019CX014).

Disease Models & Mechanisms • DMM • Accepted manuscript

References

Akagi, K., Wilson, K. A., Katewa, S. D., Ortega, M., Simons, J., Hilsabeck, T. A., Kapuria, S., Sharma, A., Jasper, H. and Kapahi, P. (2018). Dietary restriction improves intestinal cellular fitness to enhance gut barrier function and lifespan in *D. melanogaster*. *PLoS Genet* **14**, e1007777. doi:10.1371/journal.pgen.1007777

Bacchetti De Gregoris, T., Aldred, N., Clare, A. S. and Burgess, J. G. (2011). Improvement of phylum- and class-specific primers for real-time PCR quantification of bacterial taxa. *J Microbiol Methods* **86**, 351-6. doi:10.1016/j.mimet.2011.06.010

Bhandari, M., Solomon, C. G. and Swiontkowski, M. (2017). Management of acute hip fracture. *New Engl J Med* **377**, 2053-2062. doi:10.1056/NEJMcp1611090

Bhutiani, N., Li, Q., Anderson, C. D., Gallagher, H. C., De Jesus, M., Singh, R., Jala, V. R., Fraig, M., Gu, T. and Egilmez, N. K. (2018). Enhanced gut barrier integrity sensitizes colon cancer to immune therapy. *Oncoimmunology* **7**, e1498438. doi:10.1080/2162402X.2018.1498438

Blacher, E., Bashiardes, S., Shapiro, H., Rothschild, D., Mor, U., Dori-Bachash, M., Kleimeyer, C., Moresi, C., Harnik, Y., Zur, M. et al. (2019). Potential roles of gut microbiome and metabolites in modulating ALS in mice. *Nature* **572**, 474-480. doi:10.1038/s41586-019-1443-5

Britton, R. A., Irwin, R., Quach, D., Schaefer, L., Zhang, J., Lee, T., Parameswaran, N. and McCabe, L. R. (2014). Probiotic *L. reuteri* treatment prevents bone loss in a menopausal ovariectomized mouse model. *J Cell Physiol* **229**, 1822-30. doi:10.1002/jcp.24636

Browne, H. P., Forster, S. C., Anonye, B. O., Kumar, N., Neville, B. A., Stares, M. D., Goulding, D. and Lawley, T. D. (2016). Culturing of 'unculturable' human microbiota reveals novel taxa and extensive sporulation. *Nature* 533, 543-546. doi:10.1038/nature17645

Chambers, S. E. J., O'Neill, C. L., Guduric-Fuchs, J., McLoughlin, K. J., Liew, A., Egan, A. M., O'Brien, T., Stitt, A. W. and Medina, R. J. (2018). The vasoreparative function of myeloid angiogenic cells is impaired in diabetes through the induction of IL1β. *Stem Cells* **36**, 834-843. doi:10.1002/stem.2810

Chelakkot, C., Choi, Y., Kim, D. K., Park, H. T., Ghim, J., Kwon, Y., Jeon, J., Kim, M. S., Jee, Y. K., Gho, Y. S. et al. (2018). *Akkermansia muciniphila*-derived extracellular vesicles influence gut permeability through the regulation of tight junctions. *Exp Mol Med* **50**, e450. doi:10.1038/emm.2017.282

Chen, C. Y., Rao, S. S., Ren, L., Hu, X. K., Tan, Y. J., Hu, Y., Luo, J., Liu, Y. W., Yin, H., Huang, J. et al. (2018). Exosomal DMBT1 from human urine-derived stem cells facilitates diabetic wound repair by promoting angiogenesis. *Theranostics* **8**, 1607-1623. doi:10.7150/thno.22958

Chen, Y., Zhang, L., Hong, G., Huang, C., Qian, W., Bai, T., Song, J., Song, Y. and Hou, X. (2020). Probiotic mixtures with aerobic constituent promoted the recovery of multi-barriers in DSS-induced chronic colitis. *Life Sci* **240**, 117089. doi:10.1016/j.lfs.2019.117089

Cho, I., Yamanishi, S., Cox, L., Methe, B. A., Zavadil, J., Li, K., Gao, Z., Mahana, D., Raju, K., Teitler, I. et al. (2012). Antibiotics in early life alter the murine colonic microbiome and adiposity. *Nature* **488**, 621-6. doi:10.1038/nature11400

Claes, L., Recknagel, S. and Ignatius, A. (2012). Fracture healing under healthy and inflammatory conditions. *Nat Rev Rheumatol* **8**, 133-43. doi:10.1038/nrrheum.2012.1

Cottrell, J. and O'Connor, J. P. (2010). Effect of non-steroidal anti-inflammatory drugs on bone healing. *Pharmaceuticals (Basel)* **3**, 1668-1693. doi:10.3390/ph3051668

Cui, Z., Janet, Crane, J., Xie, H., Jin, X., Zhen, G., Li, C., Xie, L., Wang, L., Bian, Q., Qiu, T. et al.

Disease Models & Mechanisms • DMM • Accepted manuscript

(2016) Halofuginone attenuates osteoarthritis by inhibition of TGF-β activity and H-type vessel formation in subchondral bone. *Ann Rheum Dis*. **75**, 1714-21 doi:10.1136/annrheumdis-2015-207923

Derrien, M. (2004). *Akkermansia muciniphila* gen. nov., sp. nov., a human intestinal mucin-degrading bacterium. *Int J Syst Evol Micr* **54**, 1469-1476. doi:10.1099/ijs.0.02873-0

Derrien, M., Belzer, C. and de Vos, W. M. (2017). *Akkermansia muciniphila* and its role in regulating host functions. *Microb Pathog* **106**, 171-181. doi:10.1016/j.micpath.2016.02.005

Geerlings, S. Y., Kostopoulos, I., de Vos, W. M. and Belzer, C. (2018). *Akkermansia muciniphila* in the Human Gastrointestinal Tract: When, Where, and How? *Microorganisms* **6,** 75. doi:10.3390/microorganisms6030075

Gilbert, J. A., Blaser, M. J., Caporaso, J. G., Jansson, J. K., Lynch, S. V. and Knight, R. (2018). Current understanding of the human microbiome. *Nat Med* **24**, 392-400. doi:10.1038/nm.4517

Grander, C., Adolph, T. E., Wieser, V., Lowe, P., Wrzosek, L., Gyongyosi, B., Ward, D. V., Grabherr, F., Gerner, R. R., Pfister, A. et al. (2018). Recovery of ethanol-induced *Akkermansia muciniphila* depletion ameliorates alcoholic liver disease. *Gut* **67**, 891-901. doi:10.1136/gutjnl-2016-313432

Gu, X. N., Xie, X. H., Li, N., Zheng, Y. F. and Qin, L. J. A. B. (2012). *In vitro* and *in vivo* studies on a Mg–Sr binary alloy system developed as a new kind of biodegradable metal. *Acta Biomater* **8**, 2360-2374. doi:10.1016/j.actbio.2012.02.018

Guarner, F., and Schaafsma, G.J. (1998) Probiotics. *Int J Food Microbiol*. **39**, 237-238. doi:10.1016/s0168-1605(97)00136-0

Hayes, J. S. and Richards, R. G. (2010). The use of titanium and stainless steel in fracture fixation. *Expert Med Devic* **7**, 843-853. doi:10.1586/erd.10.53

Hu, Y., Rao, S. S., Wang, Z. X., Cao, J., Tan, Y. J., Luo, J., Li, H. M., Zhang, W. S., Chen, C. Y. and Xie, H. (2018). Exosomes from human umbilical cord blood accelerate cutaneous wound healing through miR-21-3p-mediated promotion of angiogenesis and fibroblast function. *Theranostics* **8**, 169-184. doi.org/doi:10.7150/thno.21234

Huang, J., Yin, H., Rao, S. S., Xie, P. L., Cao, X., Rao, T., Liu, S. Y., Wang, Z. X., Cao, J., Hu, Y. et al. (2018). Harmine enhances type H vessel formation and prevents bone loss in ovariectomized mice. *Theranostics* **8**, 2435-2446. doi:10.7150/thno.22144

Kaiser, K., Prystaz, K., Vikman, A., Haffner-Luntzer, M., Bergdolt, S., Strauss, G., Waetzig, G. H., Rose-John, S. and Ignatius, A. (2018). Pharmacological inhibition of IL-6 trans-signaling improves compromised fracture healing after severe trauma. *N-S Arch PharMacol* **391**, 523-536. doi:10.1007/s00210-018-1483-7

Kang, C. S., Ban, M., Choi, E. J., Moon, H. G., Jeon, J. S., Kim, D. K., Park, S. K., Jeon, S. G., Roh, T. Y., Myung, S. J. et al. (2013). Extracellular vesicles derived from gut microbiota, especially *Akkermansia muciniphila*, protect the progression of dextran sulfate sodium-induced colitis. *PLoS One* **8**, e76520. doi:10.1371/journal.pone.0076520

Kawano, M., Miyoshi, M., Ogawa, A., Sakai, F. and Kadooka, Y. (2016). *Lactobacillus gasseri* SBT2055 inhibits adipose tissue inflammation and intestinal permeability in mice fed a high-fat diet. *J Nutr Sci* **5**, e23. doi:10.1017/jns.2016.12

Kong, L., Wang, B., Yang, X., He, B., Hao, D. and Yan, L. (2020). Integrin-associated molecules and signalling cross talking in osteoclast cytoskeleton regulation. *J Cell Mol Med* **24**, 3271-3281. doi:10.1111/jcmm.15052

Disease Models & Mechanisms • DMM • Accepted manuscript

Kusumbe, A. P., Ramasamy, S. K. and Adams, R. H. (2014). Coupling of angiogenesis and osteogenesis by a specific vessel subtype in bone. *Nature* **507**, 323-328. doi:10.1038/nature13145

Lange, J., Sapozhnikova, A., Lu, C., Hu, D., Li, X., Miclau, T., 3rd and Marcucio, R. S. (2010). Action of IL-1β during fracture healing. *J Orthop Res* **28**, 778-84. doi:10.1002/jor.21061

Levy, R. M., Prince, J. M., Yang, R., Mollen, K. P., Liao, H., Watson, G. A., Fink, M. P., Vodovotz, Y. and Billiar, T. R. (2006) Systemic inflammation and remote organ damage following bilateral femur fracture requires Toll-like receptor 4. *Am J Physiol-Reg I*. **291**, R970-6. doi:10.1152/ajpregu.00793.2005

Li, J., Lin, S., Vanhoutte, P. M., Woo, C. W. and Xu, A. (2016a). *Akkermansia Muciniphila* protects against atherosclerosis by preventing metabolic endotoxemia-induced inflammation in *Apoe*$^{-/-}$ Mice. *Circulation* **133**, 2434-2446. doi:10.1161/circulationaha.115.019645

Li, J. Y., Chassaing, B., Tyagi, A. M., Vaccaro, C., Luo, T., Adams, J., Darby, T. M., Weitzmann, M. N., Mulle, J. G., Gewirtz, A. T. et al. (2016b). Sex steroid deficiency-associated bone loss is microbiota dependent and prevented by probiotics. *J Clin Invest* **126**, 2049-63. doi:10.1172/JCI86062

Lim, J. C., Ko, K. I., Mattos, M., Fang, M., Zhang, C., Feinberg, D., Sindi, H., Li, S., Alblowi, J., Kayal, R. A. et al. (2017). TNFα contributes to diabetes impaired angiogenesis in fracture healing. *Bone* **99**, 26-38. doi:10.1016/j.bone.2017.02.014

Liu, X. J., Yu, R. and Zou, K. F. (2019). Probiotic mixture VSL#3 alleviates dextran sulfate sodium-induced colitis in mice by downregulating T follicular helper cells. *Curr Med Sci* **39**, 371-378. doi:10.1007/s11596-019-2045-z

Loi, F., Cordova, L. A., Pajarinen, J., Lin, T. H., Yao, Z. and Goodman, S. B. (2016). Inflammation, fracture and bone repair. *Bone* **86**, 119-30. doi:10.1016/j.bone.2016.02.020

Meng, B., Wu, D., Cheng, Y., Huang, P., Liu, Y., Gan, L., Liu, C. and Cao, Y. (2020). Interleukin-20 differentially regulates bone mesenchymal stem cell activities in RANKL-induced osteoclastogenesis through the OPG/RANKL/RANK axis and the NF-kappaB, MAPK and AKT signalling pathways. *Scand J Immunol* **91**, e12874. doi:10.1111/sji.12874

Morhardt, T. L., Hayashi, A., Ochi, T., Quiros, M., Kitamoto, S., Nagao-Kitamoto, H., Kuffa, P., Atarashi, K., Honda, K., Kao, J. Y. et al. (2019). IL-10 produced by macrophages regulates epithelial integrity in the small intestine. *Sci Rep* **9**, 1223. doi:10.1038/s41598-018-38125-x

Mossadegh-Keller, N., Sarrazin, S., Kandalla, P. K., Espinosa, L., Stanley, E. R., Nutt, S. L., Moore, J. and Sieweke, M. H. (2013). M-CSF instructs myeloid lineage fate in single haematopoietic stem cells. *Nature* **497**, 239-43. doi: 10.1038/nature12026

Naito, Y., Uchiyama, K., and Takagi, T. (2018) A next-generation beneficial microbe: *Akkermansia muciniphila*. *J Clin Biochem Nutr*. **63**, 33-35. doi:10.3164/jcbn.18-57

Napolitano, L.M., Koruda, M.J., Meyer, A.A., and Baker, C.C. (1996) The impact of femur fracture with associated soft tissue injury on immune function and intestinal permeability. *Shock* **5**, 202-207. doi:10.1097/00024382-199603000-00006

Ohlsson, C., Engdahl, C., Fak, F., Andersson, A., Windahl, S. H., Farman, H. H., Moverare-Skrtic, S., Islander, U. and Sjogren, K. (2014). Probiotics protect mice from ovariectomy-induced cortical bone loss. *PLoS One* **9**, e92368. doi:10.1371/journal.pone.0092368

Paula, K., Katharina, S. B., Hanna, S., Timo, G., Daniel, T., Gerhard, S., Carsten, P., Frank, B. and Duda, G. N. (2010). The early fracture hematoma and its potential role in fracture healing. *Tissue Eng Part B-Re* **16**, 427-34. doi:10.1089/ten.TEB.2009.0687

Disease Models & Mechanisms • DMM • Accepted manuscript

Peng, J. H., Leng, J., Tian, H. J., Yang, T., Fang, Y., Feng, Q., Zhao, Y. and Hu, Y. Y. (2018). Geniposide and chlorogenic acid combination ameliorates non-alcoholic steatohepatitis involving the protection on the gut barrier function in mouse induced by high-fat diet. *Front Pharmacol* **9**, 1399. doi:10.3389/fphar.2018.01399

Pietschmann, P., Mechtcheriakova, D., Meshcheryakova, A., Foger-Samwald, U. and Ellinger, I. (2016). Immunology of Osteoporosis: A Mini-Review. *Gerontology* **62**, 128-37. doi:10.1159/000431091

Plovier, H., Everard, A., Druart, C., Depommier, C., Van Hul, M., Geurts, L., Chilloux, J., Ottman, N., Duparc, T., Lichtenstein, L. et al. (2017). A purified membrane protein from *Akkermansia muciniphila* or the pasteurized bacterium improves metabolism in obese and diabetic mice. *Nat Med* **23**, 107-113. doi:10.1038/nm.4236

Prystaz, K., Kaiser, K., Kovtun, A., Haffner-Luntzer, M., Fischer, V., Rapp, A. E., Liedert, A., Strauss, G., Waetzig, G. H., Rose-John, S. et al. (2018). Distinct effects of IL-6 classic and trans-signaling in bone fracture healing. *Am J Pathol* **188**, 474-490. doi:10.1016/j.ajpath.2017.10.011

Ramasamy, S. K., Kusumbe, A. P., Wang, L. and Adams, R. H. (2014). Endothelial Notch activity promotes angiogenesis and osteogenesis in bone. *Nature* **507**, 376-380. doi:10.1038/nature13146

Rao, S. S., Hu, Y., Xie, P. L., Cao, J., Wang, Z. X., Liu, J. H., Yin, H., Huang, J., Tan, Y. J., Luo, J. et al. (2018). Omentin-1 prevents inflammation-induced osteoporosis by downregulating the pro-inflammatory cytokines. *Bone Res* **6**, 9. doi:10.1038/s41413-018-0012-0

Richard, M. and Einhorn, T. A. (2011). The biology of fracture healing. *Injury* **42**, 551-555. doi.org/doi:10.1016/j.injury.2011.03.031

Schmidt-Bleek, K., Kwee, B. J., Mooney, D. J. and Duda, G. N. (2015). Boon and bane of inflammation in bone tissue regeneration and its link with angiogenesis. *Tissue Eng Part B-Re* **21**, 354-64. doi:10.1089/ten.TEB.2014.0677

Seo, S. W., Lee, D., Cho, S. K., Kim, A. D., Minematsu, H., Celil Aydemir, A. B., Geller, J. A., Macaulay, W., Yang, J. and Lee, F. Y. (2007). ERK signaling regulates macrophage colony-stimulating factor expression induced by titanium particles in MC3T3.E1 murine calvarial preosteoblastic cells. *Ann N Y Acad Sci* **1117**, 151-8. doi:10.1196/annals.1402.027

Shen, W., Shen, M., Zhao, X., Zhu, H., Yang, Y., Lu, S., Tan, Y., Li, G., Li, M., Wang, J. et al. (2017). Anti-obesity effect of capsaicin in mice fed with high-Fat diet is associated with an increase in population of the gut bacterium *Akkermansia muciniphila*. *Front Microbiol* **8**, 272. doi:10.3389/fmicb.2017.00272

Shirouchi, B., Nagao, K., Umegatani, M., Shiraishi, A., Morita, Y., Kai, S., Yanagita, T., Ogawa, A., Kadooka, Y. and Sato, M. (2016). Probiotic *Lactobacillus gasseri* SBT2055 improves glucose tolerance and reduces body weight gain in rats by stimulating energy expenditure. *Br J Nutr* **116**, 451-8. doi:10.1017/S0007114516002245

Thaler, R., Sturmlechner, I., Spitzer, S., Riester, S.M., Rumpler, M., Zwerina, J., Klaushofer, K., Wijnen, A. V. and Varga, F. (2015) Acute-phase protein serum amyloid A3 is a novel paracrine coupling factor that controls bone homeostasis. *FASEB. J.* **29**, 1344-59. doi:10.1096/fj.14-265512

Thompson, J.C., Wilson, P.G., Shridas, P., Ji, A., de Beer, M., de Beer, F.C., Webb, N. R. and Tannock, L. R. (2018) Serum amyloid A3 is pro-atherogenic. *Atherosclerosis* **268**, 32-35. doi:10.1016/j.atherosclerosis.2017.11.011

Tomlinson, R. E., McKenzie, J. A., Schmieder, A. H., Wohl, G. R., Lanza, G. M. and Silva, M. J.

Disease Models & Mechanisms • DMM • Accepted manuscript

(2013). Angiogenesis is required for stress fracture healing in rats. *Bone* **52**, 212-9. doi:10.1016/j.bone.2012.09.035

van der Lugt, B., van Beek, A. A., Aalvink, S., Meijer, B., Sovran, B., Vermeij, W. P., Brandt, R. M., de Vos, W. M., Savelkoul, H. F. and Steegenga, W. T. (2019) *Akkermansia muciniphila* ameliorates the age-related decline in colonic mucus thickness and attenuates immune activation in accelerated aging *Ercc1*$^{-/\Delta 7}$ mice. *Immun Ageing* **16**, 6. doi:10.1186/s12979-019-0145-z.eCollection 2019

Walia, B., Lingenheld, E., Duong, L., Sanjay, A. and Drissi, H. (2018). A novel role for cathepsin K in periosteal osteoclast precursors during fracture repair. *Ann N Y Acad Sci* **1415**, 57-68. doi:10.1111/nyas.13629

Wang, C., Inzana, J. A., Mirando, A. J., Ren, Y., Liu, Z., Shen, J., O'Keefe, R. J., Awad, H. A. and Hilton, M. J. (2016). NOTCH signaling in skeletal progenitors is critical for fracture repair. *J Clin Invest* **126**, 1471-81. doi:10.1172/JCI80672

Welz, P. S., Wullaert, A., Vlantis, K., Kondylis, V., Fernandez-Majada, V., Ermolaeva, M., Kirsch, P., Sterner-Kock, A., van Loo, G. and Pasparakis, M. (2011). FADD prevents RIP3-mediated epithelial cell necrosis and chronic intestinal inflammation. *Nature* **477**, 330-4. doi:10.1038/nature10273

Wing-Hoi, C., Wai-Ching, C., Ling, Q. and Kwok-Sui, L. J. J. o. O. R. (2011). Low intensity pulsed ultrasound enhances fracture healing in both ovariectomy-induced osteoporotic and age-matched normal bones. *J Orthop Res* **30**, 129-136. doi:10.1002/jor.21487

Wrba, L., Ohmann, J. J., Eisele, P., Chakraborty, S., Braumuller, S., Braun, C. K., Klohs, B., Schultze, A., Baum, H. V., Palmer, A. et al. (2018) Remote intestinal injury early after experimental polytrauma and hemorrhagic shock. *Shock* **52**, e45-e51. doi:10.1097/SHK.0000000000001271

Wu, F., Guo, X., Zhang, M., Ou, Z., Wu, D., Deng, L., Lu, Z., Zhang, J., Deng, G., Chen, S. et al. (2020). An *Akkermansia muciniphila* subtype alleviates high-fat diet-induced metabolic disorders and inhibits the neurodegenerative process in mice. *Anaerobe* **61**, 102138. doi:10.1016/j.anaerobe.2019.102138

Xie, H., Cui, Z., Wang, L., Xia, Z., Hu, Y., Xian, L., Li, C., Xie, L., Crane, J., Wan, M. et al. (2014). PDGF-BB secreted by preosteoclasts induces angiogenesis during coupling with osteogenesis. *Nature Medicine* **20**, 1270-1278, 1270-1278. doi:10.1038/nm.3668

Yin, H., Huang, J., Cao, X., Wang, Z. X., Cao, J., Hu, Y., Luo, J., Tan, Y. J., Chen, T. H., Chen, C. Y. et al. (2018). Inhibition of Src homology 2 domain-containing protein tyrosine phosphatase-2 facilitates CD31^{hi}Endomucin^{hi} blood vessel and bone formation in ovariectomized mice. *Cell Physiol Biochem* **50**, 1068-1083. doi:10.1159/000494531

Yuasa, M., Mignemi, N. A., Nyman, J. S., Duvall, C. L., Schwartz, H. S., Okawa, A., Yoshii, T., Bhattacharjee, G., Zhao, C., Bible, J. E. et al. (2015). Fibrinolysis is essential for fracture repair and prevention of heterotopic ossification. *J Clin Invest* **125**, 3117-31. doi:10.1172/JCI80313

Zhai, R., Xue, X., Zhang, L., Yang, X., Zhao, L. and Zhang, C. (2019). Strain-Specific Anti-inflammatory Properties of Two *Akkermansia muciniphila* Strains on Chronic Colitis in Mice. *Front Cell Infect Microbiol* **9**, 239. doi:10.3389/fcimb.2019.00239

Zhang, Y., Xu, J., Ruan, Y. C., Yu, M. K., O'Laughlin, M., Wise, H., Chen, D., Tian, L., Shi, D., Wang, J. et al. (2016). Implant-derived magnesium induces local neuronal production of CGRP to improve bone-fracture healing in rats. *Nat Med* **22**, 1160-1169. doi:10.1038/nm.4162

Disease Models & Mechanisms • DMM • Accepted manuscript

Figures

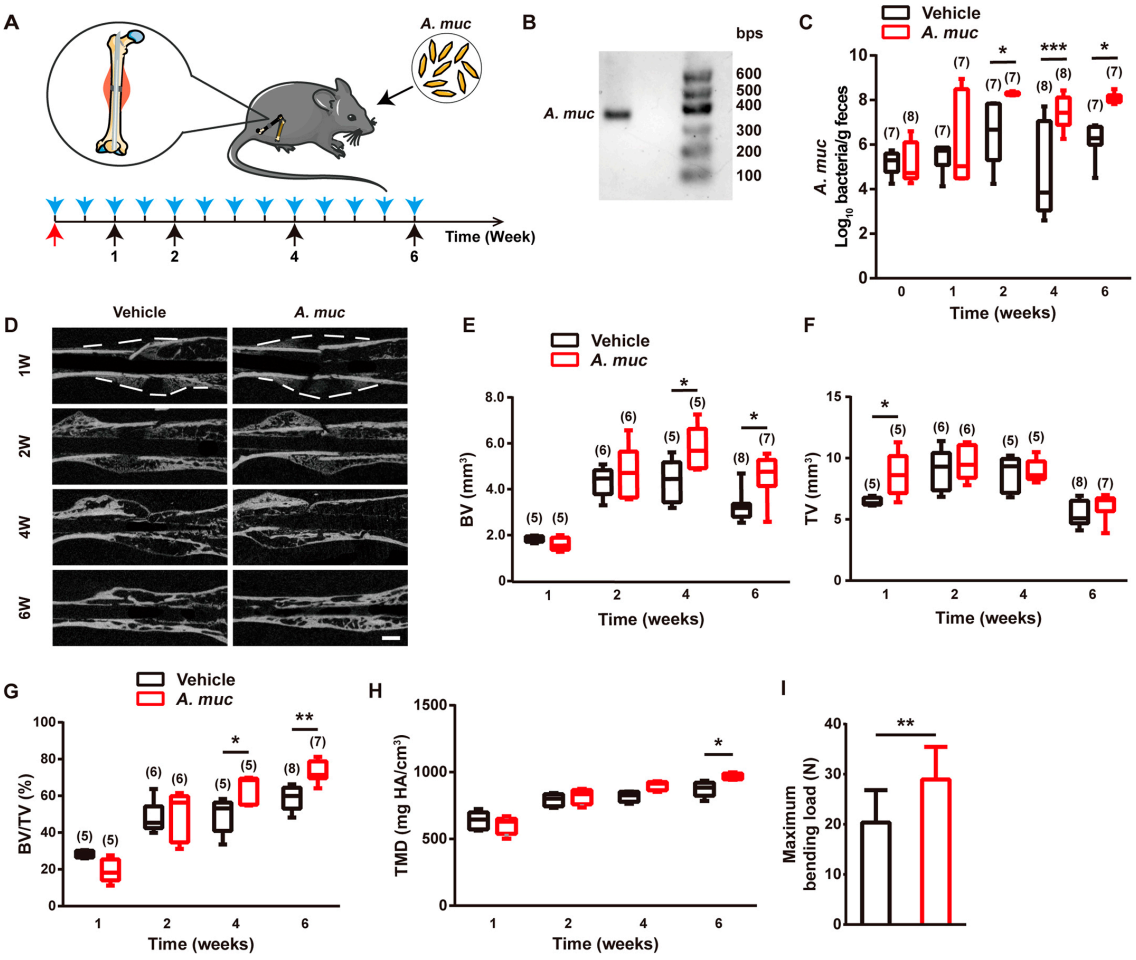

Fig. 1. *A. muc* treatment accelerates fracture healing. (A) Experiment design for testing the impact of *A. muc* on fracture healing. Blue arrows indicate *A. muc* administrations. Red arrow indicates fracture surgery. Black arrows indicate time points to sacrifice mice. (B) Amplifed *A. muc* DNA band detected by agarose gel electrophoresis. (C) Abundances of *A. muc* in fecal samples were examined by qRT-PCR. *n* of each group is shown in parentheses. (D) Representative µCT images of fractured femora from vehicle- or *A. muc*-treated mice at different time points. Scale bar: 1 mm. (E-G) µCT quantitative analyses of BV (E), TV (F) and BV/TV (G) of fractured femora at 1, 2, 4 and 6 WPF. *n* of each group is shown in parentheses. (H) Tissue mineral density (TMD) of callus at 1, 2, 4 and 6 WPF. $n = 5$ per group. (I) Four-point bending measurement of femoral ultimate load at 6 WPF. $n = 10$ per group. For C and E-H, $^{*}P < 0.05$, $^{**}P < 0.01$, $^{***}P < 0.001$ by two-way ANOVA with Bonferroni *post hoc* test. For I, $^{**}P < 0.01$ by unpaired two tailed Student's *t* test.

Disease Models & Mechanisms • DMM • Accepted manuscript

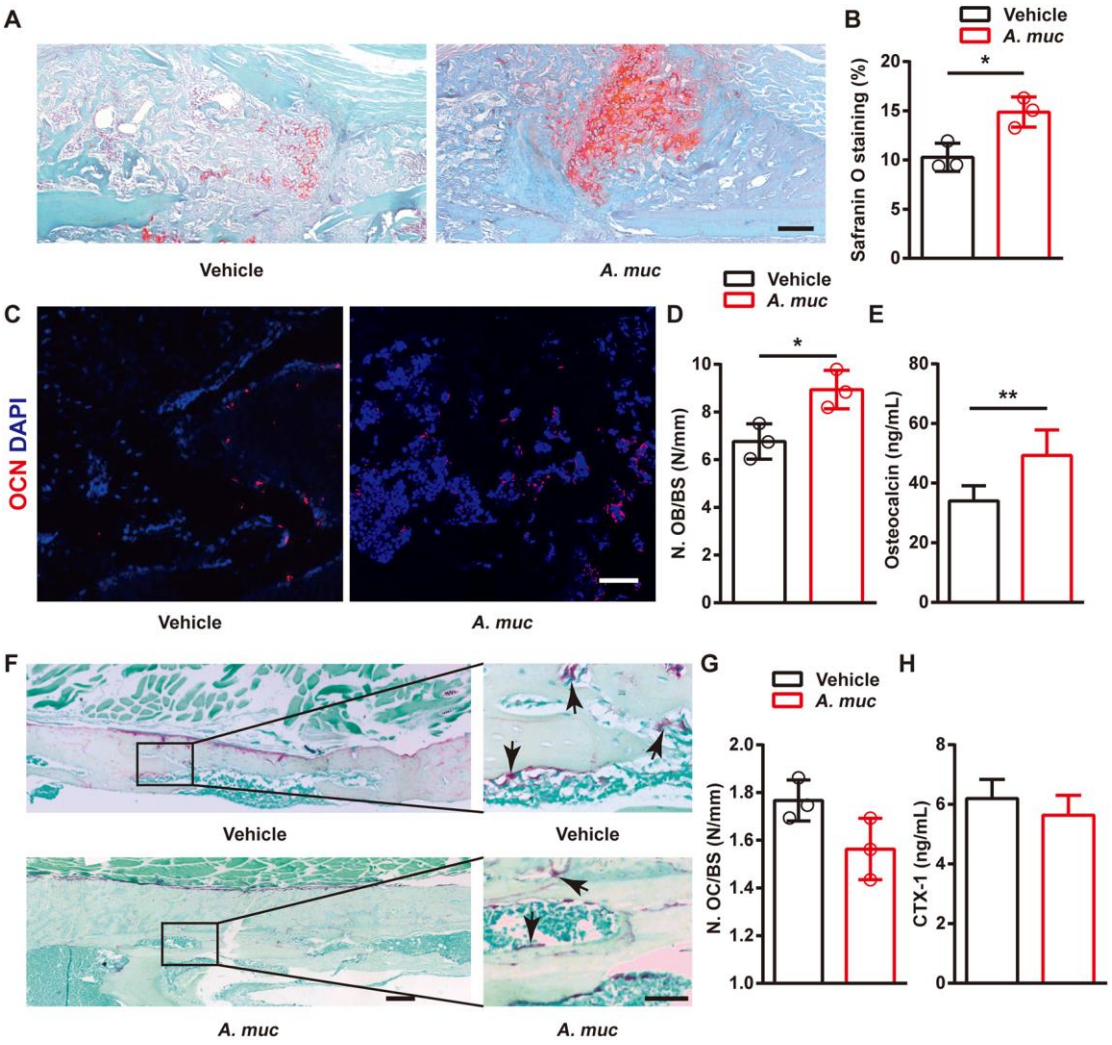

Fig. 2. The effects of *A. muc* treatment on chondroid callus formation, osteogenesis and osteoclastogenesis in fractured femora of mice. (A,B) Representative images of safranin O staining (A) and of quantification of positive-stained area (B) in fractured femora from vehicle- or *A. muc*-treated mice at 2 WPF. n = 3 per group. Scale bar: 100 µm. (C,D) Representative OCN-stained sections (C) with quantification of osteoblast number (N. OB) (D) in fractured femora from vehicle- or *A. muc*-treated mice at 6 WPF. n = 3 per group. Scale bar: 50 µm. (E) Serum concentrations of OCN detected by ELISA at 6 WPF. n = 6 per group. (F,G) Representative TRAP-stained sections (F) with quantification of osteoclast number (N. OC) (G) in fractured femora from vehicle- or *A. muc*-treated mice at 6 WPF. Arrows indicate osteoclasts. Scale bar: 200 µm (left), 50 µm (right). n = 3 per group. (H) Serum concentrations of CTX-1 detected by ELISA at 6 WPF. n = 6 per group. $^{*}P < 0.05$, $^{**}P < 0.01$ by unpaired two tailed Student's t test.

Disease Models & Mechanisms • DMM • Accepted manuscript

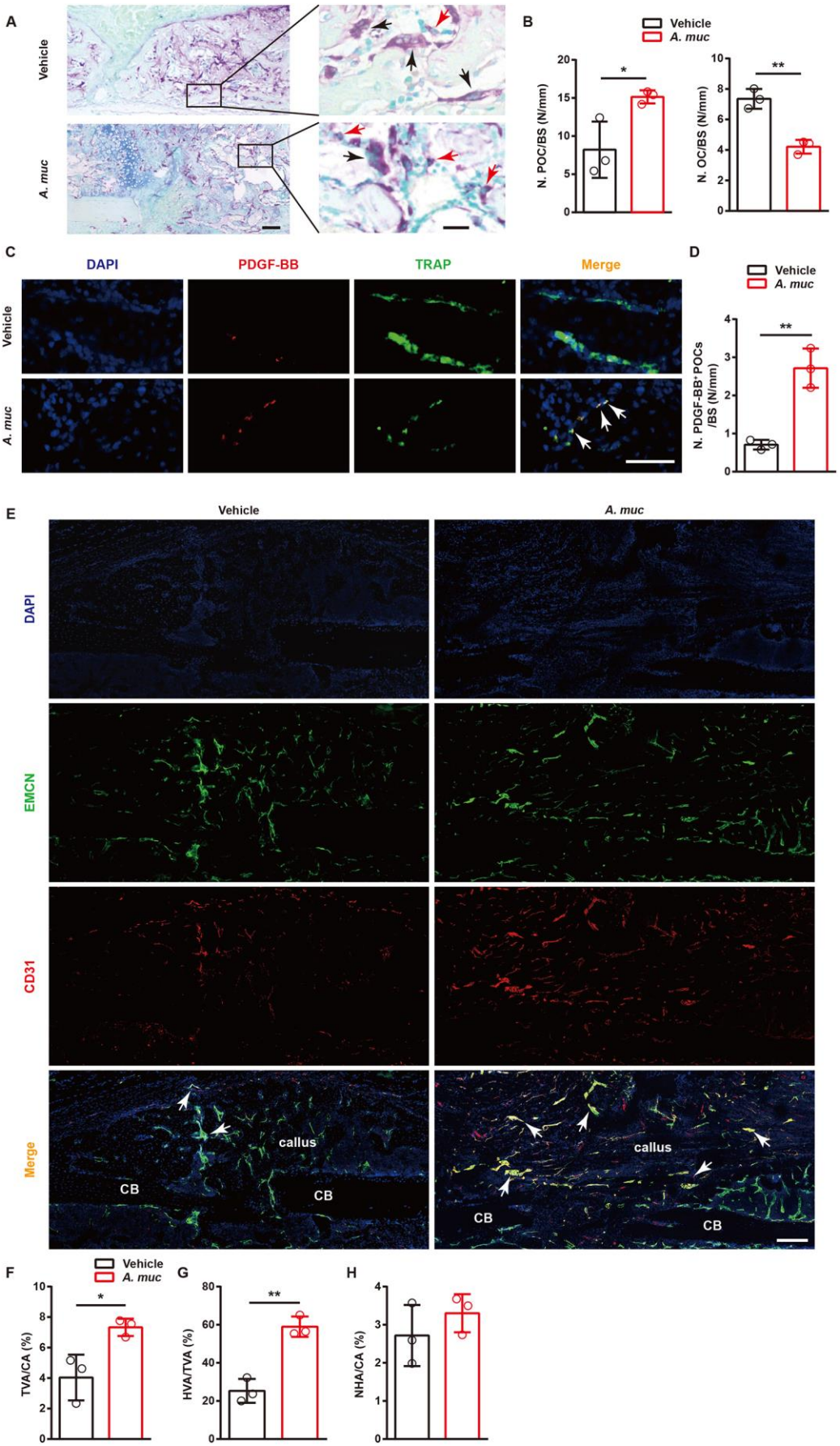

Disease Models & Mechanisms • DMM • Accepted manuscript

Fig. 3. *A. muc* supplementation stimulates preosteoclasts and type H vessels formation in fractured femora of mice. (A,B) Representative images of TRAP-staining (A) with quantification of preosteoclast number (N. POC, left) and osteoclast number (N. OC, right) (B) at 2 WPF. Black arrows indicate osteoclasts and red arrows indicate preosteoclasts. BS: bone surface. n = 3 per group. Scale bar: 200 μm (left), 20μm (right). (C,D) Representative images of $TRAP^+$ (green) and $PDGF\text{-}BB^+$ (red) coimmunostaining (C) with quantification of $PDGF\text{-}BB^+$ preosteoclast ($TRAP^+$ mononuclear cells) number (D) at 2 WPF. Arrows indicate $PDGF\text{-}BB^+$ preosteoclast cells. n = 3 per group. Scale bar: 50μm. (E-H) Representative images of CD31 and Emcn coimmunostaining (E) with quantification of the ratio of total vessels area (TVA) (F), type H vessels area (HVA) (G) and none-type H vessels area (NHA) (H) at 2 WPF. Arrows indicate type H vessels. CA: callus area. CB: cortical bone. Scale bar: 200 μm. n = 3 per group. $^{*}P < 0.05$, $^{**}P < 0.01$ by unpaired two tailed Student's t test.

Disease Models & Mechanisms • DMM • Accepted manuscript

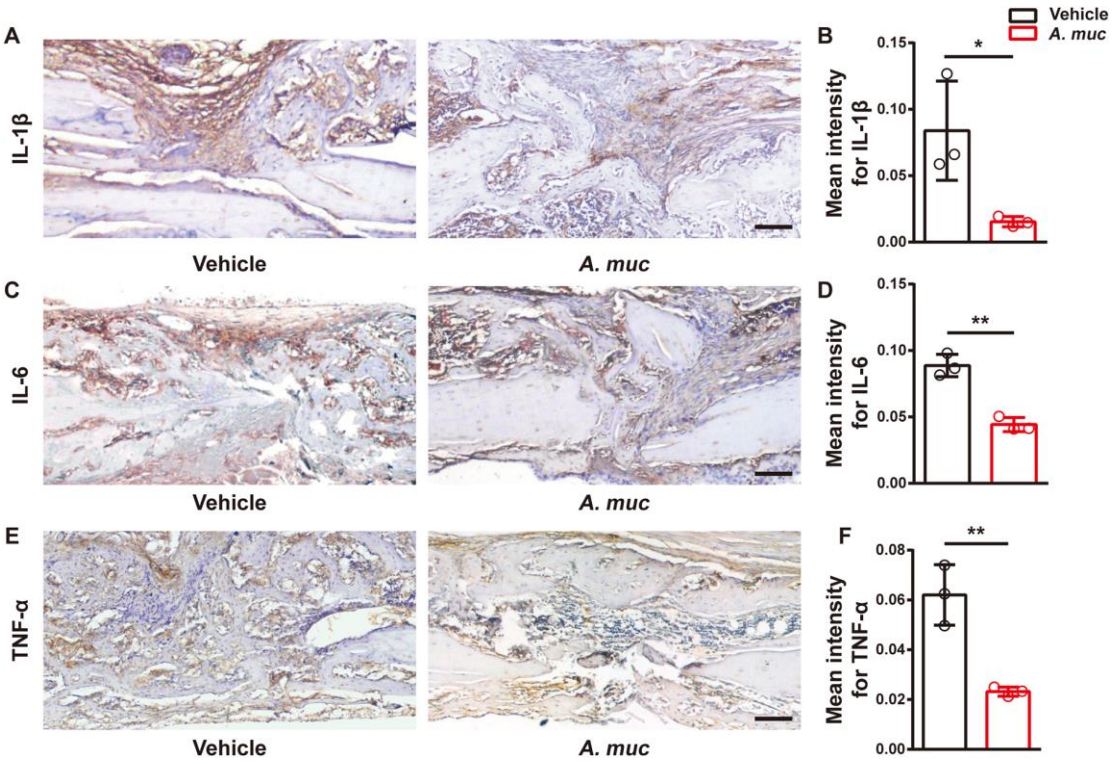

Fig. 4. *A. muc* treatment alleviates local inflammatory responses in fractured femora of mice. (A,B) Representative images (A) and quantitative analyses (B) of immunohistochemical staining for IL-1β at 2 WPF. $n = 3$ per group. Scale bar: 100 µm. (C,D) Representative images (C) and quantitative analyses (D) of immunohistochemical staining for IL-6 at 2 WPF. $n = 3$ per group. Scale bar: 100 µm. (E,F) Representative images (E) and quantitative analyses (F) of immunohistochemical staining for TNF-α at 2 WPF. $n = 3$ per group. Scale bar: 100 µm. $^{*}P < 0.05$, $^{**}P < 0.01$ by unpaired two tailed Student's *t* test.

Disease Models & Mechanisms • DMM • Accepted manuscript

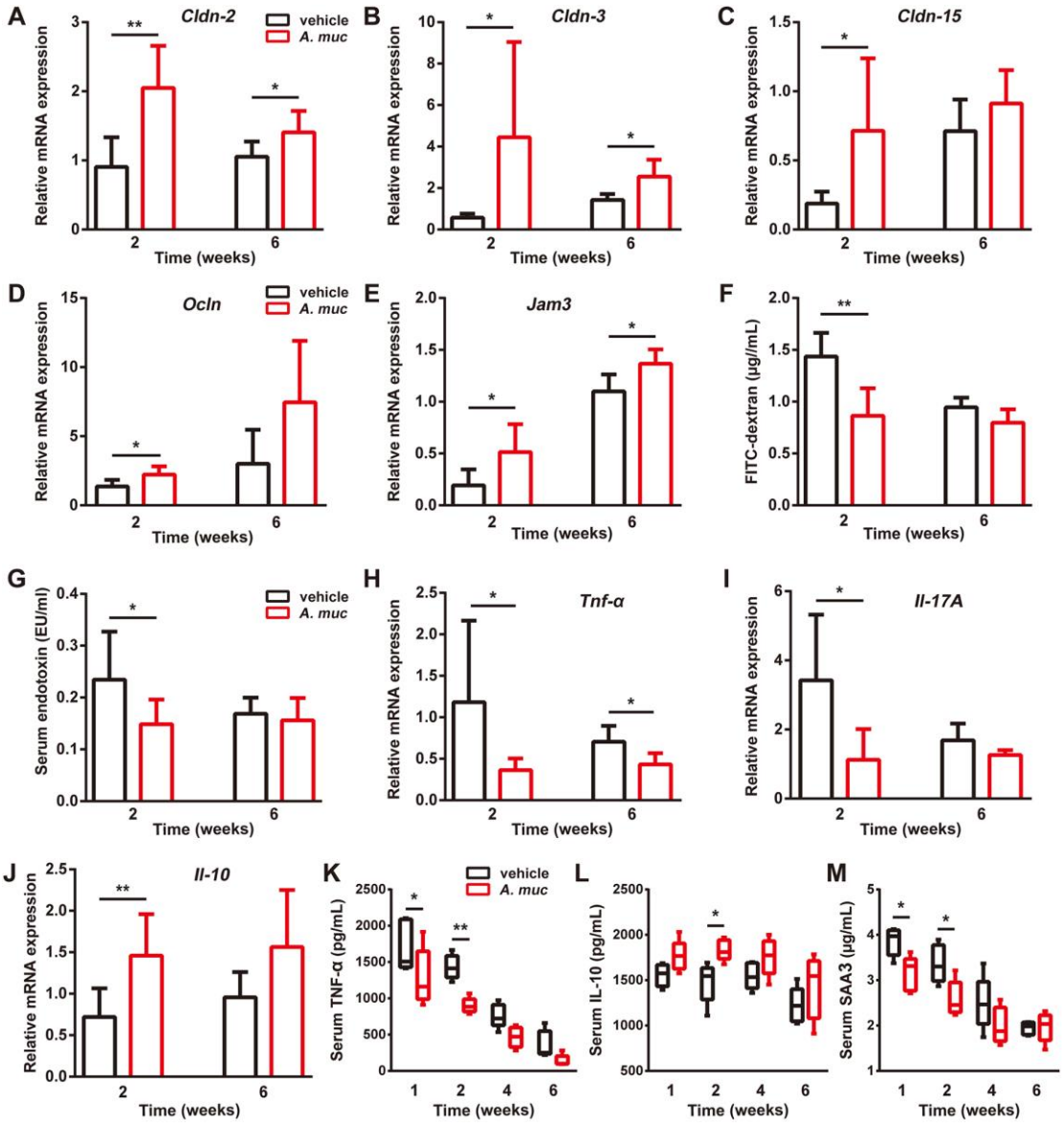

Fig. 5. *A. muc* administration tightens the gut barrier and reduces systemic inflammation in the femur fracture mouse model. (A-E) qRT-PCR measurements of colonic mRNA levels of *Cldn-2*, *-3* and *-15*, as well as of *Ocln* and *Jam3* at 2 and 6 WPF. For 2 weeks, $n = 6$ per group, for 6 weeks, $n = 7$ per group. (F) Serum FITC-dextran levels were measured 4 hours after FITC-dextran oral administration at 2 and 6 WPF. $n = 5$ per group. (G) LPS levels in serum samples at 2 and 6 WPF. $n = 8$ per group. (H-J) qRT-PCR analyses of colonic mRNA levels of *Tnf-α*, *Il-17A* and *Il-10* at 2 and 6 WPF. For 2 weeks, $n = 6$ per group, for 6 weeks, $n = 7$ per group. (K-M) Serum concentrations of TNF-α (K), IL-10 (L) and SAA3 (M) detected by ELISA at 1, 2, 4 and 6 WPF. $n = 5$ per group. For A-J, $^{*}P < 0.05$, $^{**}P < 0.01$ by unpaired two tailed Student's *t* test. For K-M, $^{*}P < 0.05$, $^{**}P < 0.01$ by two-way ANOVA with Bonferroni *post hoc* test.

Disease Models & Mechanisms • DMM • Accepted manuscript

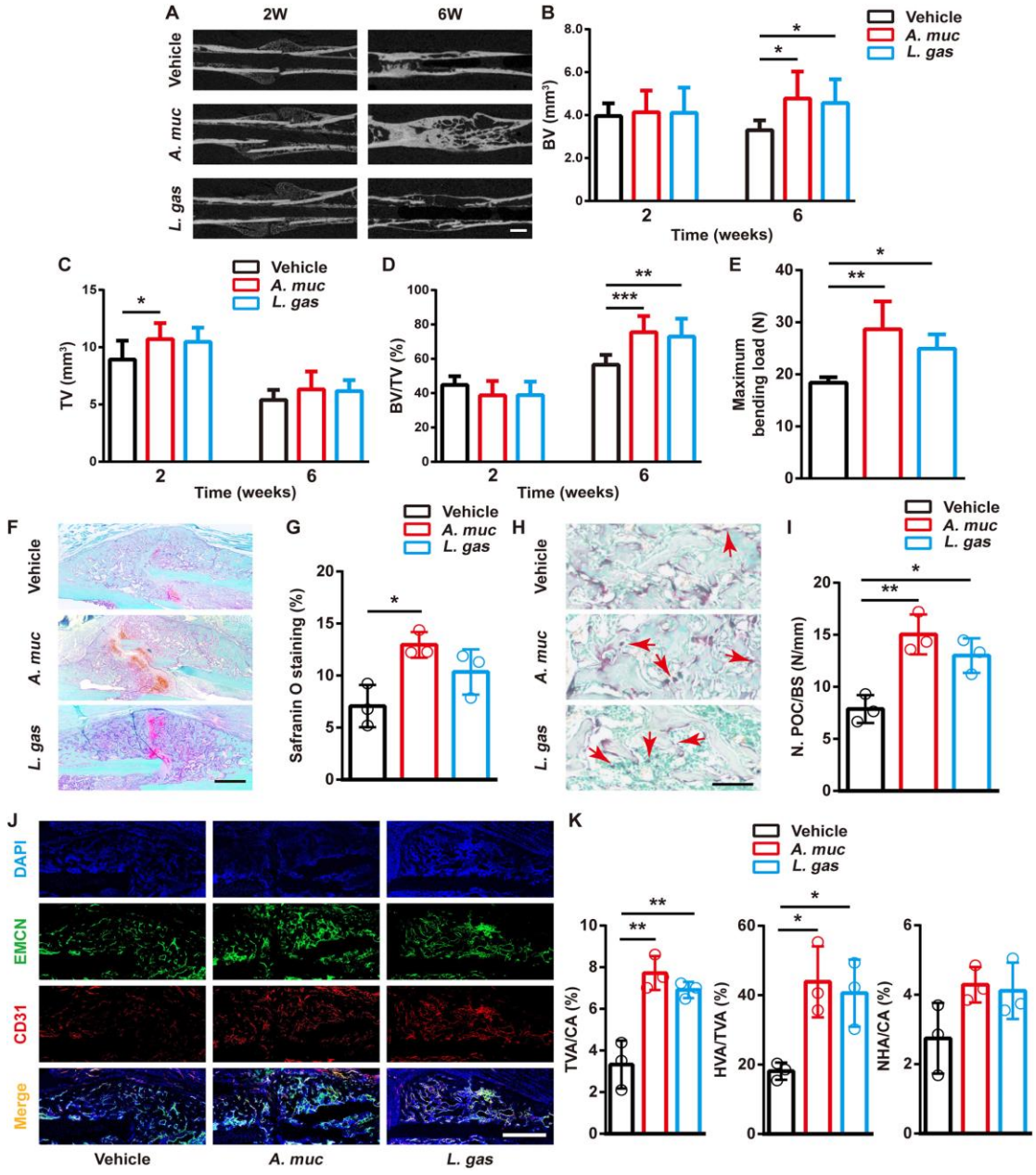

Fig. 6. Supplementation of probiotics promotes bone repair and angiogenesis. (A) Representative µCT images of fractured femora from vehicle-, *A. muc*- and *L. gas*-treated mice at 2 and 6 weeks. Scale bar: 1 mm. (B-D) µCT quantitative analyses of BV (B), TV (C) and BV/TV (D) of fractured femora at 2 and 6 WPF. n = 8 per group. (E) Four-point bending measurement of femoral ultimate load at 6 WPF. n = 5 per group. (F,G) Representative images of safranin O staining (F) and of quantification of positive-stained area (G) in fractured femora at 2 WPF. n = 3 per group. Scale bar: 200 µm. (H,I) Representative images of TRAP-staining (H) with quantification of preosteoclast number (N. POC) (I) at 2 WPF. Red arrows indicate preosteoclasts. BS: bone surface. n = 3 per group. Scale bar: 50µm. (J,K) Representative images of CD31 and Emcn coimmunostaining (J) with quantification (K) of the ratio of total vessels area (TVA), type H vessels area (HVA) and none-type H vessels area (NHA) at 2 WPF. Scale bar: 500 µm. n = 3 per group. $^{*}P < 0.05$, $^{**}P < 0.01$, $^{***}P < 0.001$ by one-way ANOVA with Bonferroni *post hoc* test.

Disease Models & Mechanisms • DMM • Accepted manuscript

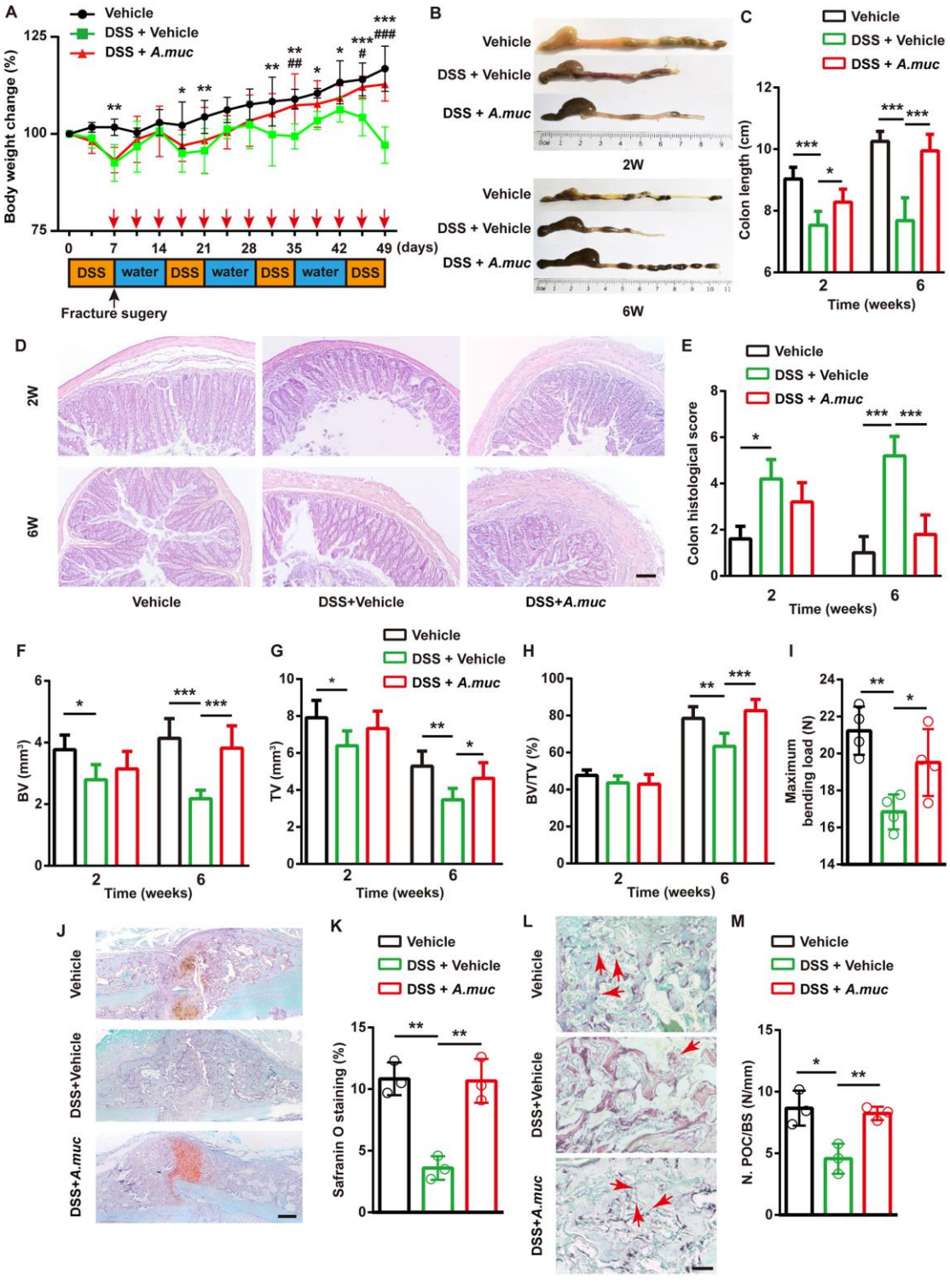

Fig. 7. *A. muc* protected against DSS-induced impairment on fracture healing. (A) Experimental design for DSS treatment and body weight change of mice. Red arrows indicate *A. muc* administration. Black arrow indicates fracture surgery. n = 6 per group. (B,C) Representative images of colons (B) with quantification of colon length at 2 and 6 WPF (C). n = 6 per group. (D,E) Representative images of HE staining of colon at 2 and 6 WPF (D) with quantification of histological scores (E). n = 5 per group. Scale bar: 100 μm. (F-H) μCT quantitative analyses of

Disease Models & Mechanisms • DMM • Accepted manuscript

BV (F), TV (G) and BV/TV (H) of fractured femora at 2 and 6 WPF. n = 6 per group. (I) Four-point bending measurement of femoral ultimate load at 6 WPF. n = 4 per group. (J,K) Representative images of safranin O staining (J) and of quantification of positive-stained area (K) in fractured femora at 2 WPF. n = 3 per group. Scale bar: 100 µm. (L,M) Representative images of TRAP-staining (L) with quantification of preosteoclast number (N. POC) (M) at 2 WPF. Red arrows indicate preosteoclasts. BS: bone surface. n = 3 per group. Scale bar: 20 µm. For A, two-way ANOVA with Bonferroni *post hoc* test was used to perform multiple-group comparisons, $^{*}P < 0.05$, $^{**}P < 0.01$, $^{***}P < 0.001$, DSS + vehicle group vs. Vehicle group, $^{\#}P < 0.05$, $^{\#\#\#}P < 0.001$ DSS + vehicle group vs. DSS + *A. muc* group. For C, E, F-I, K and M, $^{*}P < 0.05$, $^{**}P < 0.01$, $^{***}P < 0.001$ by unpaired two tailed Student's *t* test.

Disease Models & Mechanisms • DMM • Accepted manuscript

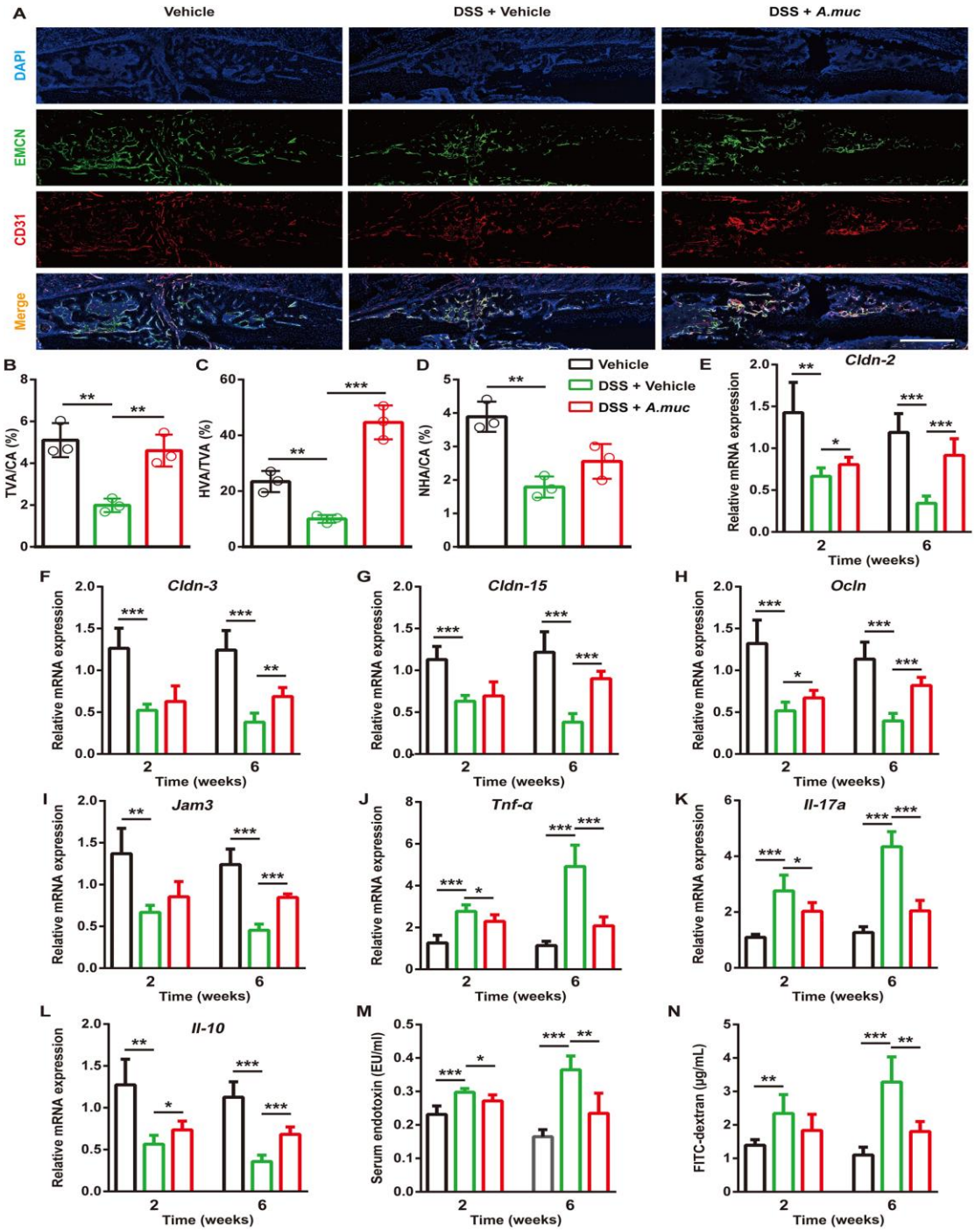

Fig. 8. *A. muc* treatment restores the type H vessels formation and decreases gut permeability of DSS-treated mice. (A-D) Representative images of CD31 and Emcn coimmunostaining (A) with quantification of the ratio of total vessels area (TVA), type H vessels area (HVA) and none-type H vessels area (NHA) (L) at 2 WPF. Scale bar: 500 μm. $n = 3$ per group. (E-L) qRT-PCR measurements of colonic mRNA levels of *Cldn-2*, *-3* and *-15*, *Ocln*, *Jam3*, *Tnf-α*, *Il-17A* and *Il-10* at 2 and 6 WPF. $n = 5$ per group. (M) LPS levels in serum samples at 2 and 6 WPF. $n = 5$ per group. (N) Serum FITC-dextran levels were measured 4 hours after FITC-dextran oral administration at 2 and 6 WPF. $n = 5$ per group. $^{*}P < 0.05$, $^{**}P < 0.01$, $^{***}P < 0.001$ by unpaired two tailed Student's *t* test.

Disease Models & Mechanisms • DMM • Accepted manuscript

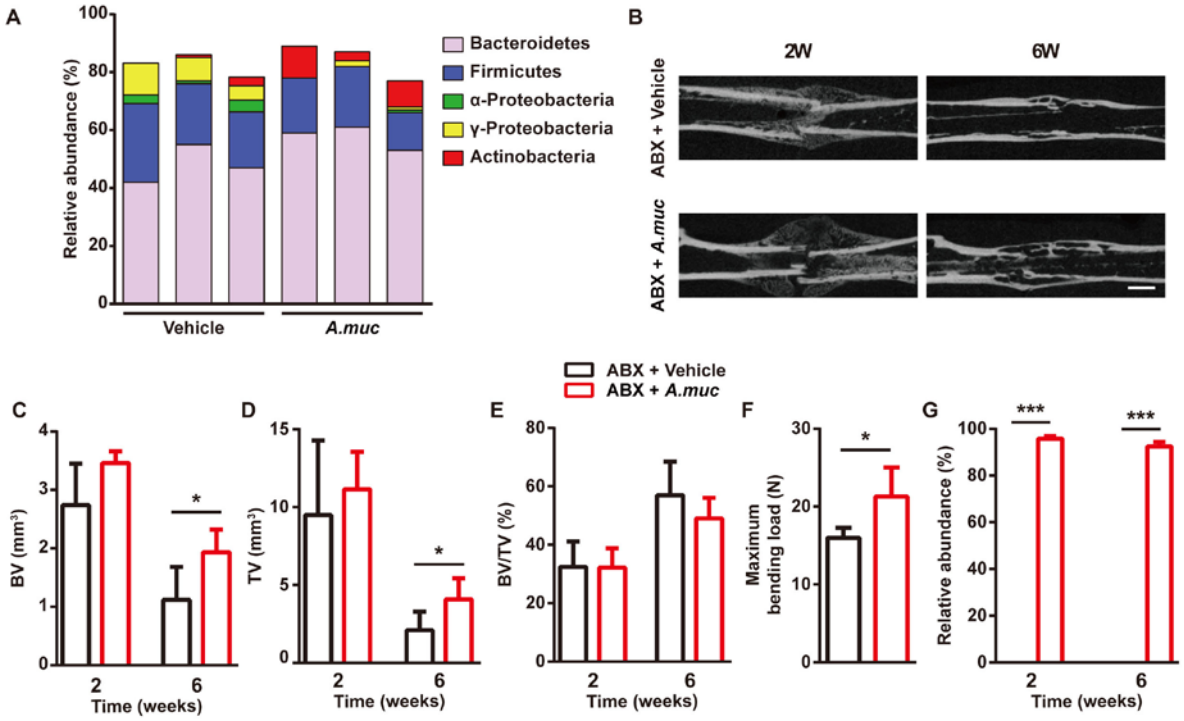

Fig. S1. *A. muc* improves bone repair in gut microbiota-depleted mice. (A) Fecal microbiota composition of vehicle-treated group and *A. muc*-treated group evaluated by 16S rDNA qRT-PCR. $n = 3$ per group. (B) Representative µCT images of fractured femora from ABX + vehicle and ABX + *A. muc* group mice at 2 and 6 weeks. Scale bar: 1 mm. (C-E) µCT quantitative analyses of BV (C), TV (D) and BV/TV (E) of fractured femora at 2 and 6 WPF. $n = 5$ per group. (F) Four-point bending measurement of femoral ultimate load at 6 WPF. $n = 5$ per group. (G) Abundances of *A. muc* in fecal samples of ABX + vehicle and ABX + *A. muc* group mice. $n = 5$ per group. $^{*}P < 0.05$, $^{***}P < 0.001$ by unpaired two tailed Student's *t* test.

Disease Models & Mechanisms • Supplementary information

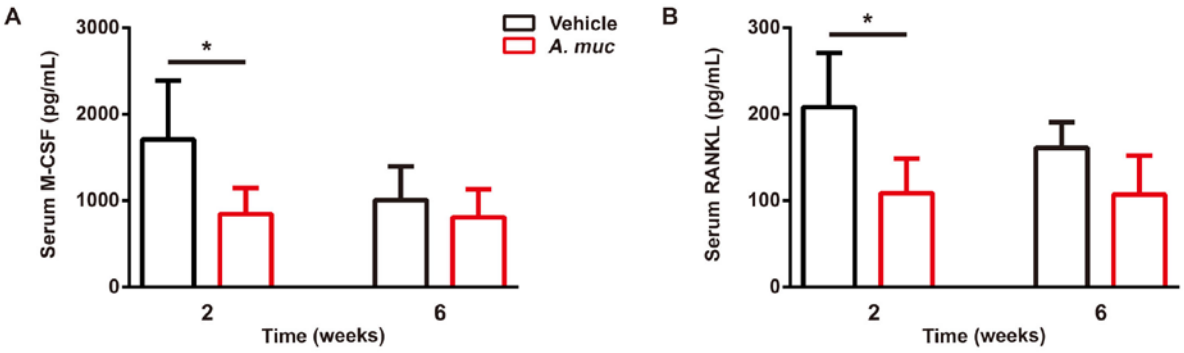

Fig. S2. *A. muc* decreases circulatory levels of M-CSF and RANKL. (A) Serum concentrations of M-CSF (A) and RANKL (B) detected by ELISA at 2 and 6 WPF. $n = 5$ per group. $^{*}P < 0.05$ by unpaired two tailed Student's t test.

Disease Models & Mechanisms • Supplementary information

Table S1: Primers used for 16S rDNA qRT-PCR in Figure S1

Target group	Primer sequence
Universal	AAACTCAAAKGAATTGACGG CTCACRRCACGAGCTGAC
α-Proteobacteria	CIAGTGTAGAGGTGAAATT CCCCGTCAATTCCTTTGAGTT
γ-Proteobacteria	TCGTCAGCTCGTGTYGTGA CGTAAGGGCCATGATG
Bacteroidetes	CRAACAGGATTAGATACCCT GGTAAGGTTCCTCGCGTAT
Firmicutes	TGAAACTYAAAGGAATTGACG ACCATGCACCACCTGTC
Actinobacteria	TACGGCCGCAAGGCTA TCRTCCCCACCTTCCTCCG

Disease Models & Mechanisms • Supplementary information

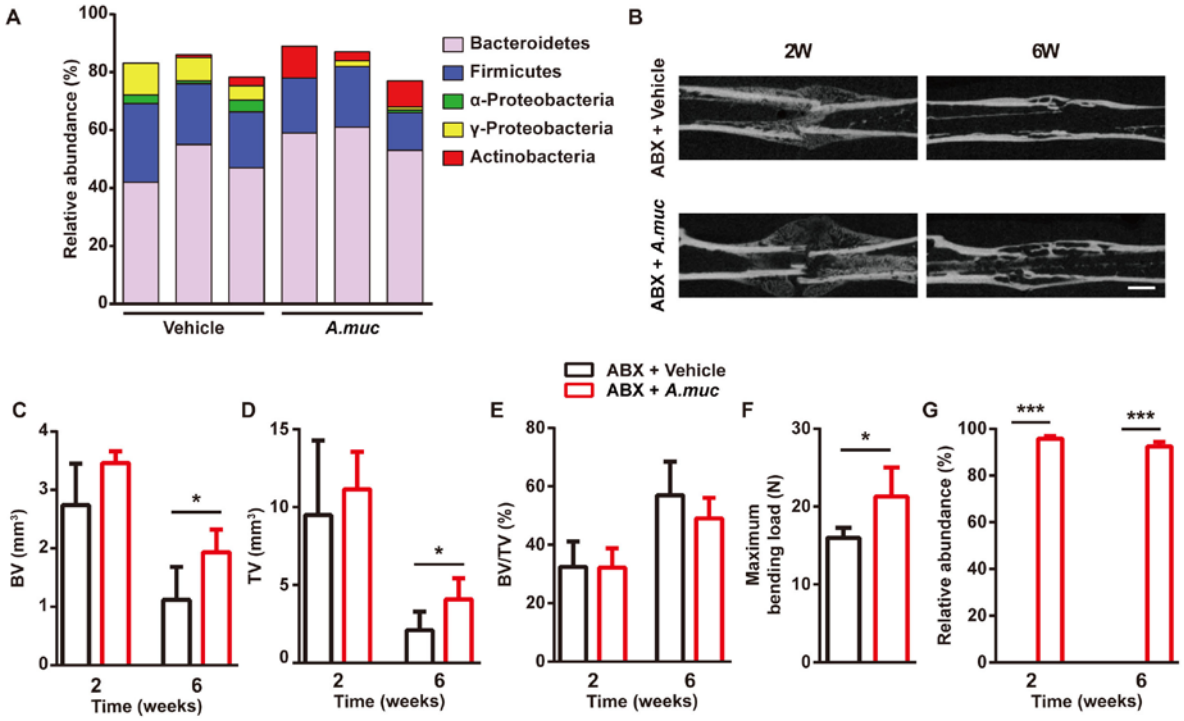

Fig. S1. *A. muc* improves bone repair in gut microbiota-depleted mice. (A) Fecal microbiota composition of vehicle-treated group and *A. muc*-treated group evaluated by 16S rDNA qRT-PCR. $n = 3$ per group. (B) Representative µCT images of fractured femora from ABX + vehicle and ABX + *A. muc* group mice at 2 and 6 weeks. Scale bar: 1 mm. (C-E) µCT quantitative analyses of BV (C), TV (D) and BV/TV (E) of fractured femora at 2 and 6 WPF. $n = 5$ per group. (F) Four-point bending measurement of femoral ultimate load at 6 WPF. $n = 5$ per group. (G) Abundances of *A. muc* in fecal samples of ABX + vehicle and ABX + *A. muc* group mice. $n = 5$ per group. $^{*}P < 0.05$, $^{***}P < 0.001$ by unpaired two tailed Student's *t* test.

Disease Models & Mechanisms • Supplementary information

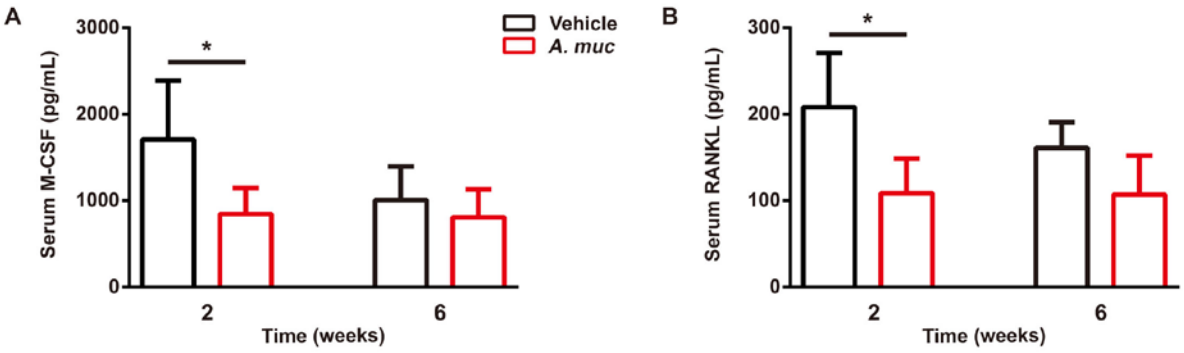

Fig. S2. *A. muc* decreases circulatory levels of M-CSF and RANKL. (A) Serum concentrations of M-CSF (A) and RANKL (B) detected by ELISA at 2 and 6 WPF. $n = 5$ per group. $^{*}P < 0.05$ by unpaired two tailed Student's t test.

Disease Models & Mechanisms • Supplementary information

Table S1: Primers used for 16S rDNA qRT-PCR in Figure S1

Target group	Primer sequence
Universal	AAACTCAAAKGAATTGACGG CTCACRRCACGAGCTGAC
α-Proteobacteria	CIAGTGTAGAGGTGAAATT CCCCGTCAATTCCTTTGAGTT
γ-Proteobacteria	TCGTCAGCTCGTGTYGTGA CGTAAGGGCCATGATG
Bacteroidetes	CRAACAGGATTAGATACCCT GGTAAGGTTCCTCGCGTAT
Firmicutes	TGAAACTYAAAGGAATTGACG ACCATGCACCACCTGTC
Actinobacteria	TACGGCCGCAAGGCTA TCRTCCCCACCTTCCTCCG

Disease Models & Mechanisms • Supplementary information